Colloidal quantum dots for optoelectronics

Houtepen, A. J.; Sargent, E. H.; Infante, I.; Owen, J. S.; Green, P. B.; Schaller, R. D.; Bals, S.; Zeiske, Stefan; Stöferle, T.; Hens, Z.

DOI
10.1038/s43586-025-00413-y

Publication date
2025

Document Version
Final published version

Published in
Nature Reviews Methods Primers

Citation (APA)
Houtepen, A. J., Sargent, E. H., Infante, I., Owen, J. S., Green, P. B., Schaller, R. D., Bals, S., Zeiske, S., Stöferle, T., & Hens, Z. (2025). Colloidal quantum dots for optoelectronics. *Nature Reviews Methods Primers*, *5*(1), Article 42. https://doi.org/10.1038/s43586-025-00413-y

nature reviews methods primers

https://doi.org/10.1038/s43586-025-00413-y

Primer

Check for updates

Colloidal quantum dots for optoelectronics

A. J. Houtepen[1], E. H. Sargent[2,3], I. Infante[4,5], J. S. Owen[6], P. B. Green[7,8], R. D. Schaller[2,9], S. Bals[10,11], Stefan Zeiske[2], T. Stöferle[12] & Z. Hens[7,8]

Abstract

Colloidal quantum dots (QDs) are semiconductor nanocrystals that have unique size-tunable optoelectronic properties and are suitable for wet processing. QD research aims to answer fundamental questions about the chemical and physical properties of nanoscale materials and use these tools for technological applications ranging from bio-imaging to quantum optics. At the core of this field is a set of synthetic, processing and analytical methods designed to produce QDs in uniform ensembles that meet the highest performance standards. This Primer reviews QD fabrication methods with a focus on the applications of QDs in printed optoelectronics and quantum optics. After outlining the current state-of-the-art QD syntheses, the experimental and computational analysis of QDs is discussed. These topics are then connected to the methodologies, processes and concepts required for developing QD-based photodetectors, light-emitting devices and quantum optics applications. Special attention is paid to challenges in reproducibility and current limitations of the field, such as the need to balance non-restricted material composition with high performing technology while achieving long-term stability in QD devices under operating conditions. Finally, the ongoing advancement in QD synthesis, precise atomic-level analysis and computational methodologies are highlighted as key drivers towards rational QD design, particularly in understanding how structural changes under loading impact QD properties.

Sections

A full list of affiliations appears at the end of the paper. ✉e-mail: zeger.hens@ugent.be

Introduction

Quantum dots (QDs) are nanometre-sized semiconductor crystallites in which the energies of electrons and excitons are governed by nanocrystal size and shape, a phenomenon known as quantum confinement[1–3]. Wet chemical methods enable QDs to be synthesized by precipitation reactions yielding colloidal dispersions of QDs. QD research advanced tremendously after the discovery that adjusting the balance between nucleation and growth in a colloidal synthesis allows for the production of large batches of QDs with precisely controlled size and shape[4]. Access to semiconductor nanocolloids with tunable optoelectronic properties sparked an extensive research effort into the fundamental aspects of size quantization[5] and inspired the formation of QD devices by wet-processing methods, such as spin coating, bar coating or inkjet printing[6] (Supplementary Information 1). Figure 1 illustrates how various technologies resulted from QD solution processibility, including solar cells and photodectors[7], colour-converted and electroluminescent light-emitting diodes (LEDs)[8,9], luminescent solar concentrators (LSCs)[10], optically pumped lasers[11], electrically pumped superluminescent LEDs[12] and initial milestones in quantum technology[13]. Notably, QD-based devices derived from this research often address gaps in contemporary technology, such as QD-enhanced displays providing unmatched colour rendering[14] and infrared (IR) imagers offering a low-cost alternative to existing systems and new capabilities for multispectral imaging[15].

QD technology requires QDs of the highest quality. Initially, the most-used QDs involved Cd-based II–VI and Pb-based IV–VI chalcogenides for applications involving visible (Vis) and IR light, respectively. Later, research was extended to Pb-based perovskites for their excellent optical properties[16], In-based III–V pnictides and Cu-based I–III–VI$_2$ chalcopyrites, which fully comply with regulations on hazardous substances[17], and Zn-based and Hg-based II–VI chalcogenides to cover ultraviolet (UV) and mid-IR wavelengths[18]. The potential of these different QDs can be evaluated using various figures of merit. As listed in Table 1, these include typical linear characteristics of optical materials, such as the photoluminescence quantum yield (PLQY) and the emission linewidth. Applications in lasing and quantum optics, by contrast, require more specific properties, such as the biexciton lifetime and the exciton dephasing time, which are summarized in Table 2. Achieving the most desirable properties for a given application relies on a high level of control over QD synthesis and careful modifications of the QD surface. For instance, forming core/shell heterostructures can suppress non-radiative recombination of electron–hole pairs through passivation of surface-localized trap states[19]. Replacing long organic ligands – typical as-synthesized surface terminations – with shorter moieties enhances charge-carrier mobility in QD assemblies[20], whereas a graded core/shell interface reduces non-radiative recombination of biexcitons by impeding Auger recombination[21].

This Primer surveys the key methods required for producing high-quality QDs, with an emphasis on essential concepts and insights. Starting from the latest progress in QD synthesis, experimental and computational methods to determine the atomistic structure, surface composition and optoelectronic properties of QDs are discussed. Although examples are taken from literature on CdSe, InP, CsPbBr$_3$ and PbS QDs, which have been most extensively researched, many results can be generalized to a broader range of QDs. Material synthesis and analysis are then connected to advancements in QD processing and the development of colour conversion, printed optoelectronics and quantum applications. This Primer addresses the reproducibility and limitations of current methods, emphasizing the need for QDs composed of high-performance materials that are stable under operational conditions and not subject to toxicity restrictions. With continued progress in QD synthesis, precise atomic-scale analysis and computational methodology, there is a promising outlook for rational QD design.

Experimentation

As outlined in Fig. 1, the discovery of the hot injection synthesis of cadmium chalcogenides gave rise to a range of synthetic protocols for the formation of QDs with different compositions, heterostructures or shapes. In parallel, studies addressed the chemical mechanisms of the underlying reactions, proposing strategies for size control and addressing the problem of polydispersity. This section covers these general, mechanistic insights. A more exhaustive overview of synthesis protocols is provided in Supplementary Information 2.

Quantum dot synthesis methods

A QD synthesis typically starts from (I) precursors that react to form solutes, followed by the precipitation of these soluble building blocks into crystals by (II) nucleation and (III) growth (Fig. 2a). Typically, this synthesis is implemented through the swift injection of one or more precursors into the hot surfactant mixture, a process known as hot injection. Reaction conditions, including the composition of the reaction mixture as well as the injection and reaction temperature, are designed to produce an ensemble of QDs with a narrow size distribution. In this respect, hot injection was seen as implementing La Mer's canonical model of particle formation[22], in which monodisperse colloids are obtained through a burst of nucleation that is initiated by the supersaturation of solutes formed by the precursor conversion (Fig. 2b). In line with Fig. 2a, the (I) buildup of supersaturation is caused by the formation of solutes from the precursor conversion reaction and leads to crystallization through (II) nucleation and (III) growth. Furthermore, the average size of the QD ensemble can (IV) evolve after completion of the precursor conversion through ripening, which can induce unwanted broadening of the size distribution. Many successful examples exist, however, of QD syntheses that slowly heat the precursors and surfactants to the synthesis temperature or gradually add precursors using a syringe pump. Such methods are inherently more scalable and produce size distributions that rival those of hot injection techniques[23].

As outlined in Supplementary Information 2, a range of synthetic procedures has been developed, leading to monodisperse QD batches that are optically active across a broad range of wavelengths (Table 1). Even so, reproducing these results can be difficult as the purity of synthetic precursors and specificity of reaction conditions can strongly affect QD formation. Thus, improving QD syntheses typically relies on empirical optimization, in which synthetic design is only weakly linked to the accepted mechanism of QD formation. Better mechanistic insight can, however, support the development of even higher performing materials at larger scale and improve the understanding of the relation between QD structure and function.

Size control by balancing nucleation and growth kinetics. The reaction between precursors is an essential component of QD synthesis. Its reliability affects synthetic reproducibility as it governs the balance between nucleation and growth stages by controlling the supply rate, Q, of soluble building blocks. Sugimoto et al.[24] argued that at the moment nucleation stops, the solute supply rate matches the QD growth rate (the rate at which building blocks are incorporated in

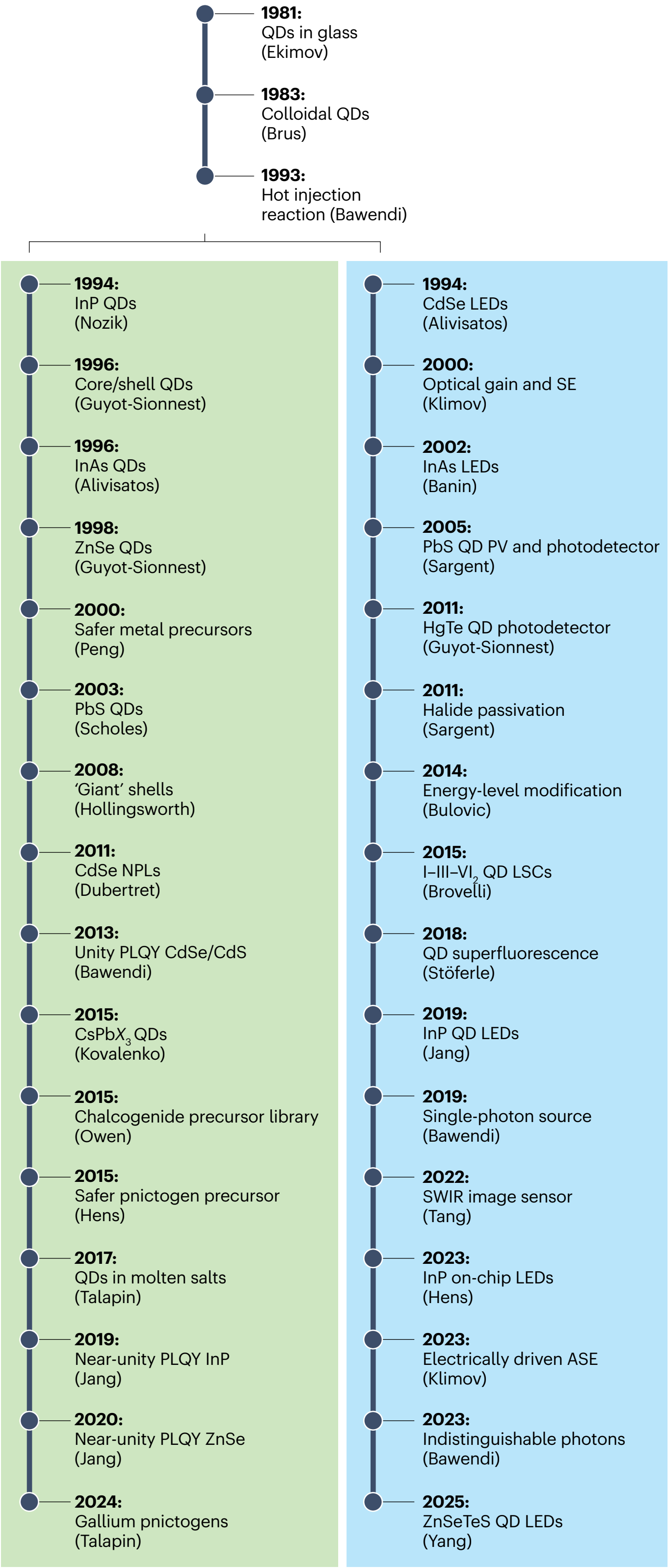

Fig. 1 | Timeline highlighting the development of quantum dot synthesis and technology. This timeline follows the evolution of quantum dot (QD) synthesis and technology from the initial discovery of quantum confinement to precision methods for colloidal QD synthesis (green track) and QD-based optoelectronics (blue track). ASE, amplified spontaneous emission; LED, light-emitting diode; LSC, luminescent solar concentrator; NPL, nanoplatelet; PLQY, photoluminescence quantum yield; PV, photovoltaic; SE, stimulated emission; SWIR, short-wave infrared.

existing QDs). The supply rate is given by the product of the growth rate G per QD and the number of crystals n:

$$Q = G \times n. \tag{1}$$

Equation (1) explains how the interplay among solute supply, nucleation and growth can be leveraged to adjust the QD size. An inverse relation exists between the final number of QDs produced during nucleation and the growth rate, meaning that faster growth kinetics lead to fewer nuclei and larger final sizes. Similarly, the solute supply kinetics can tune the extent of nucleation. Reactive precursors that supply solutes more rapidly will promote nucleation – producing a higher n at fixed G – and thus decrease the QD size[25].

Several classes of reagents derived from phosphine chalcogenides[25,26], chalcogenoureas[27,28], dichalcogenides[29] and aminophosphines[30] have been used to provide orders of magnitude differences in the conversion reactivity and study its impact on size control. Moreover, independent control over the conversion reactivity allows the temperature of the synthesis and the solute supply to be decoupled, and the influence of temperature on the nucleation and growth stages to be isolated from the precursor reaction[30,31].

Formation of monodisperse quantum dot batches. Although size control determines the range of wavelengths accessible to QDs of a single material (λ_X in Table 1), monodisperse QD batches show a minimal spread around a single wavelength ($\Delta\lambda_X$ in Table 1), thereby emitting more monochromatic colours or enhancing charge-carrier mobility. According to La Mer's model, solute supply creates a supersaturated mixture in which a burst of nucleation quickly establishes an ensemble of crystals that then grow slowly in unison[22] (Fig. 2b). The monodispersity of the ensemble results from the short nucleation period that separates the nucleation and growth stages in time. Alternatively, monodisperse distributions can result from size-dependent growth kinetics that narrow the polydispersity during growth, a process commonly called size focusing.

Size-dependent growth kinetics are a natural consequence of mass transport limitations when growth is limited by the kinetics of solute diffusion to the crystal rather than the kinetics of solute attachment to its surface. Solutes become depleted near the QD surface, which induces an inverse dependence of G on the QD radius as outlined in Fig. 2c. Under such conditions, the faster growth of smaller QDs will focus the size distribution as the ensemble of sizes grows[32]. The broad acceptance of this mechanism, and the assumption of size-independent attachment kinetics, led numerous groups to explain the narrowing of the QD optical spectrum by diffusion-limited growth mechanisms[33]. However, direct evidence of diffusion-limited growth of QDs is lacking, and estimates of the growth rate constant are orders of magnitude smaller than diffusion in studies of CdSe and PbS[34,35]. Similarly, although explaining QD synthesis through burst

Table 1 | Figures of merit related to absorption or emission of light for different classes of quantum dots

Material	λ_X (nm)	$\Delta\lambda_X$ (nm)	PLQY (%)	$\mu_{i\ 450}$ (10^5 cm^{-1})	Applications
CdSe-based structures (λ_{gap} ~715 nm, d_{conf} ~6 nm)					
CdSe QD[a]	430–650	20–30	~100 (refs. 251,252)	0.81	QD colour conversion (LCDs, on-chip LEDs, microLEDs), QLEDs, QD lasers, QD-LSCs
CdSe/ZnS QD[b]	450–650	21 (515 nm)	88 (515 nm)[253]	0.093	
CdSe/CdS QD[c]	560–650	20–25	95 (ref. 251)	0.75	
CdSe NPL[d]	393–643	~10	50 (core) 90 (core/crown)	NA	
InP-based structures (λ_{gap} ~915 nm, d_{conf} ~14 nm)					
InP/ZnSe/ZnS QDs[e]	500–700	35–40	100 (630 nm)[9]	0.48[f]	QD colour conversion (LCDs, on-chip LEDs, microLEDs), QLEDs
InP/ZnSe/ZnS QDs[g]	480–650	45–50	90–95 (ref. 56)	0.48[f]	
CsPbBr$_3$ structures (λ_{gap} ~525 nm, d_{conf} ~6 nm)					
CsPbBr$_3$ QDs	440–520 (ref. 254)	15–25	~100 (ref. 255)	0.87 (ref. 256)	QD colour conversion (LCDs, on-chip LEDs, microLEDs), QLEDs
ZnSe-based structures (λ_{gap} ~470 nm)					
ZnSe/ZnS QDs	350–440	<10 (ref. 257)	95 (ref. 257)	0.052	QLEDs
CuInS$_2$-based structures (λ_{gap} ~830 nm)					
CuInS$_2$/ZnS QDs	500–1,000 (ref. 258)	100 (650 nm)	85 (ref. 259)	Unknown	QD-LSCs
PbS-based structures (λ_{gap} ~3,000 nm, d_{conf} ~45 nm)					
PbS QDs	600–3,000 (refs. 260,261)	150 (1,500 nm)	40–80 (1,500 nm)[262]	1.15	QD solar cells, IR imagers, QD-LEDs
InAs-based structures (λ_{gap} ~3,400 nm)					
InAs QDs[h]	900–1,600 (ref. 263)	100 (ref. 263)	<1 (ref. 263)	1.50	IR imagers, QD-LEDs
InAs/InP/ZnSe QDs[i]	750–1,100 (ref. 264)	60–75 (ref. 264)	40–80 (ref. 264)	0.67[j]	
InAs/ZnSe QDs[h]	900 (ref. 265)	135 (ref. 265)	70 (ref. 265)	0.65[j]	
HgTe structures (zero-gap bulk compound, d_{conf} ~73 nm)					
HgTe QDs	700–100,000 (ref. 18)	130 (ref. 266) (1,200 nm)	75 (ref. 266) (1,200 nm)	2.14	IR imagers, QD-LEDs

Semiconductors are characterized by the wavelength λ_{gap} corresponding to the bulk band-edge absorption wavelength and the upper diameter d_{conf} that characterizes the strong confinement regime[55]. The intrinsic absorption coefficient, $\mu_{i,450}$, at 450 nm is calculated using bulk optical constants, a core volume fraction of 10% and toluene as the solvent[267]. For CsPbB$_3$, experimental values at 450 nm are given. IR, infrared; LCD, liquid crystal display; LED, light-emitting diode; LSC, luminescent solar concentrator; NA, not available; NPL, nanoplatelet; PLQY, photoluminescence quantum yield; QD, quantum dot; QLED, quantum light-emitting diode. [a]PLQY strongly depends on surface chemistry. [b]Mostly for green emission. [c]Mostly for red emission. [d]Wavelength range for 2.5–9.5 monolayers. [e]Synthesis by tris-trimethyl-silylphosphine. [f]Without ZnS outer shell. [g]Synthesis by tris-diethyl-aminophosphine. [h]Synthesis by tris-trimethyl-silylarsine. [i]Synthesis by tris-dimethyl-aminoarsine. [j]Without ZnSe outer shell.

nucleation is common practice, this mechanism is not well supported by experiments[36].

The size and size dispersion of a growing QD ensemble can be measured using in situ small-angle X-ray scattering or ex situ optical measurements (Supplementary Information 2). Combining both methods, recent studies found a long nucleation stage that substantially overlaps with the growth process[30,35,37,38]. These findings clearly contrast with the argument that La Mer's burst nucleation drives the narrow polydispersity typical of QDs. The narrow size distribution observed under those conditions therefore must arise from size distribution focusing during growth.

Interestingly, those studies also argue that the size distribution focusing is not caused by diffusion-limited growth but by the reactivity of the surface towards the attachment of solutes. To size focus, the reactivity of the QD surface towards solute attachment must decrease as the size grows. Various mechanisms could explain the size dependence of the growth kinetics of nanocrystals, such as size-dependent facet nucleation[39,40], ligand penetration[41] and size-dependent ligand binding[42,43] (Fig. 2d). These are new explanations of size focusing with little precedent, as surface reaction-limited growth is typically argued to be size-independent. Importantly, the reduced surface reactivity of larger QDs towards growth causes the extended nucleation, which counteracts monodispersity[38]. Translating these mechanistic insights in practical synthesis protocols should, therefore, address a better separation of nucleation from growth and optimize the size dependence of the reactivity towards growth.

Growth by ripening. In the absence of solute generation from precursor conversion, the QD size can still evolve through ripening. As depicted in Fig. 2e, the ensemble can cannibalize itself by the exchange of monomers, shrinking some crystals to grow others, a process known as Ostwald ripening. Typically, Ostwald ripening is associated with the slow and steady increase in size and polydispersity of a QD ensemble. Interestingly, the inverse process has also been observed, which narrows the size distribution and increases the surface area of the ensemble, as first reported by Klabunde and co-workers[44] in studies of gold. This so-called digestive ripening can be triggered by exposing QDs to a surfactant ligand and heat, after which a broad distribution of large sizes narrows down and shrinks to smaller average size. Although digestive ripening of gold in thiol solution is well established, recent reports indicate that digestive ripening can also be used to improve the polydispersity and to reduce the size of metal chalcogenide and perovskite QDs[45–47].

The simultaneous reduction in diameter and narrowing are an apparent violation of the Gibbs–Thompson relationship, which argues that the surface tension is reduced as the average size increases and the total surface area drops. That discrepancy is an indication that strong ligand–surface bonding in QDs can lead to enthalpically favourable surface energies. Similar arguments can explain the stability of the so-called magic-size clusters, as shown in Fig. 2f. Both examples indicate that ligand stabilization of the QD surface is an important component of polydispersity control and presents a new angle to achieve QDs with molecule-like homogeneity.

Results

QDs are hybrid objects, combining a crystalline inorganic core with a surface often terminated by organic ligands. The interplay between core and surface determines the optoelectronic properties of QDs, and establishing this relationship between structure and property requires a broad range of analytical techniques, from determining the QD geometry to understanding the relaxation of photo-excited QDs. This section provides an overview of the most important methods for experimental and computational QD analysis, with additional background contained in Supplementary Information 3–8.

Quantum dot characterization

Advances in colloidal synthesis have yielded semiconductor nanocrystals with a broad range of geometries. Zero-dimensional (0D) QDs, featuring strong confinement in three directions, can be made as quasi-spheres, cubes or tetrahedrons. One-dimensional quantum rods with confinement in two directions or 2D quantum wells confined in one direction can be obtained with narrow size dispersion[48,49] (Supplementary information 2). In addition, multistep reactions have been developed to form epitaxial heterostructures, such as 0D core/shells[19], 1D dot-in-rod[50] or 2D core/crown structures[51]. Standard QD characterization, therefore, involves data on elemental composition, size and shape and crystal structure. Moreover, given the strong relation between QD geometry and optoelectronic properties, such studies are always combined with optical spectroscopy. Absorption spectroscopy, for example, provided the first evidence of quantum confinement in semiconductor nanocrystals as manifested by a blue-shifted band-edge transition with a reduction in QD size[1,52–54], and now sizing curves provide a rapid way of converting band-edge energy into a QD size[55].

Figure 3 displays an example of various characterization methods for InP/ZnSe core/shell QDs[56]. Lower magnification transmission electron microscopy (TEM) images provide an overview of the distribution of sizes and shapes within the QD ensemble, whereas high-resolution TEM yields more detailed insights in crystallinity. Crystallinity can be further confirmed through powder X-ray diffraction (XRD), which shows diffraction mostly in line with bulk ZnSe, which dominates the QD volume. Small-angle X-ray scattering and total scattering can provide further insights in the QD size and atomic structure[31,57] (Supplementary Information 3). Opposite from the XRD pattern, the Raman

Table 2 | Figures of merit relevant for QD lasing and quantum optics applications for different classes of QDs

Material	λ_X (nm)	$\tau_{X,\mathrm{rad}}$ (293 K, ns)	$\tau_{X,\mathrm{rad}}$ (5 K, ns)	$\tau_{\mathrm{BX,Auger}}$ (ns)	$T_{2,X}$ (ns)	Single-photon purity (293 K)
CdSe-based structures (λ_{gap} ~715 nm, d_{conf} ~6 nm)						
CdSe QD[a]	430–650	20–25 (ref. 268)	Unknown	0.006–0.3 (ref. 269)	Unknown	Unknown
CdSe/ZnS QD[b]	450–650	25 (ref. 270)	6 (ref. 271)	0.006–0.3	0.109 (FWM)[272]	0.004 (ref. 273)
CdSe/CdS QD[c]	560–650	>25 (ref. 274)	3.6–7.1 (ref. 275) (dot-in-rod)	0.3–1.6 (ref. 276); 1–100 (ref. 21)	0.110 (FWM)[215]	0.07 (ref. 277)
CdSe NPL	393–643	4 (ref. 48)	0.1 (ref. 123)	NA	0.001 (FWM)[217]	Unknown
InP-based structures (λ_{gap} ~915 nm, d_{conf} ~14 nm)						
InP/ZnSe/ZnS QDs[d]	500–700	Unknown	Unknown	Unknown	0.25 (PCFS)[151]	0.077–0.086 (ref. 151)
InP/ZnSe/ZnS QDs[e]	480–650	30–40 (ref. 278)	21–38 (ref. 126)	0.06 (ref. 278)	0.023 (FWM)[279]	0.03–0.4 (ref. 280)
$CsPbBr_3$-based structures (λ_{gap} ~525 nm, d_{conf} ~6 nm)						
$CsPbBr_3$ QDs[f]	440–520	4–5 (refs. 97,281)	0.1–0.3 (ref. 282) (>10 nm NCs)	0.012 (ref. 97) (~5 nm QDs)	0.08 (PCFS)[218], 0.0245 (FWM)[216]	0.085–0.4 (ref. 196)
PbS-based structures (λ_{gap} ~3,000 nm, d_{conf} ~45 nm)						
PbS QDs	850–3,000	1,000–2,000 (ref. 262)	Unknown	0.035 (ref. 283)	<0.001 (FWM)[284]	0.4 (ref. 285)
InAs-based structures (λ_{gap} ~3,400 nm)						
InAs/ZnSe QDs	900 (ref. 265)	50–55 (ref. 265)	Unknown	Unknown	Unknown	Unknown

Semiconductors are characterized by the wavelength λ_{gap} corresponding to the bulk band-edge absorption wavelength and the upper diameter d_{conf} that characterizes the strong confinement regime[55]. FWM, four-wave mixing; NA, not available; NC, nanocrystal; NPL, nanoplatelet; PCFS, photon-correlation Fourier spectroscopy; QD, quantum dot. [a]$\tau_{\mathrm{BX,Auger}}$ scales with QD volume. [b]$\tau_{\mathrm{BX,Auger}}$ presumed equal to CdSe QDs. [c]$\tau_{X,\mathrm{rad}}$ scales with core and shell size. [d]Synthesis by tris-trimethyl-silylphosphine. [e]Synthesis by tris-diethyl-aminophosphine. [f]Radiative rate at 5 K scales with NC volume.

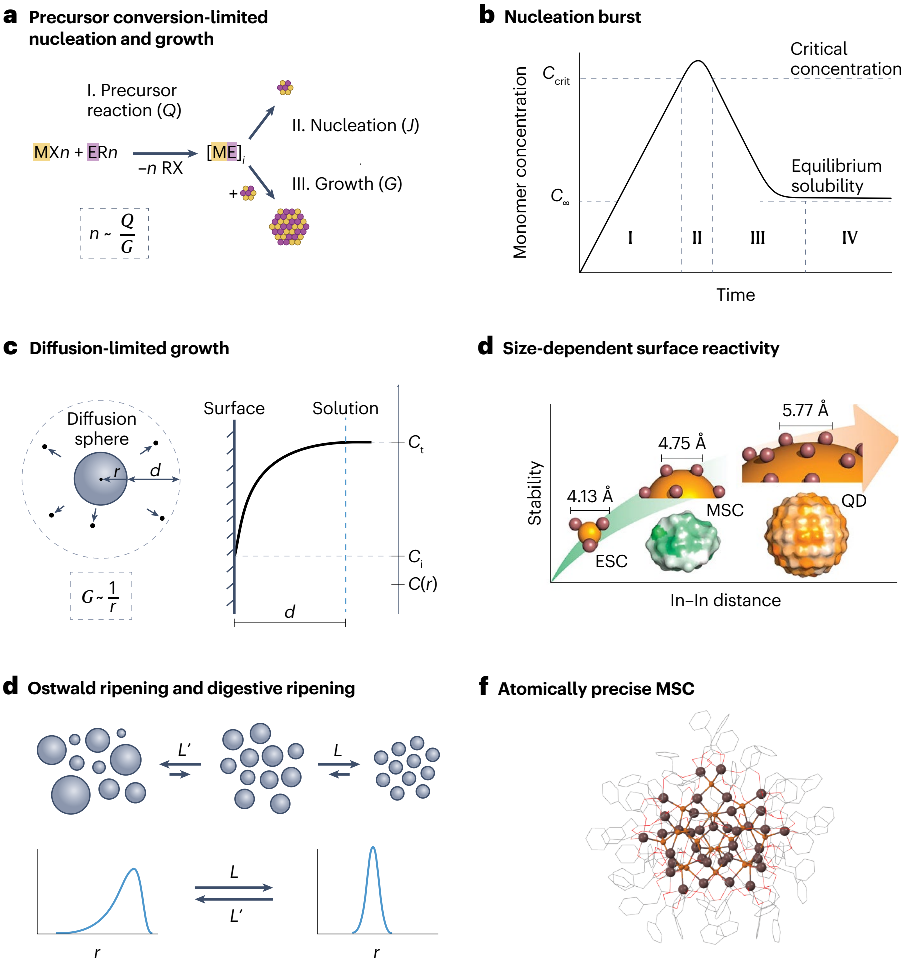

Fig. 2 | Quantum dot synthesis steps. a, Breakdown of quantum dot (QD) formation with (I) precursor decomposition, (II) nucleation and (III) growth (*n*, number of QDs; *Q*, precusor decomposition rate; *G*, growth rate per QD). **b**, Representation of the La Mer model as a sequence of the I–III reaction steps, followed by (IV) ripening (*C*, solute concentration). **c**,**d**, Illustration of diffusion-limited (part **c**) and reaction-limited (part **d**) growth as two mechanisms for size focusing. **e**, Ostwald and digestive ripening as surface energy-minimization processes leading to a broadening or a narrowing of the size distribution. **f**, A magic-size cluster (MSC) as a unique atomic arrangement that minimizes surface energy. ESC, early-stage cluster. Panel **d** adapted with permission from ref. 43, American Chemical Society. Panel **f** adapted with permission from ref. 109, American Chemical Society.

spectrum features separate modes of the InP core and the ZnSe shell. Shifts with respect to InP-only or ZnSe-only modes can be related to compressive and tensile strain[58]. The average elemental composition can be obtained not only through Rutherford backscattering spectrometry on QD films but also through inductively coupled plasma-optical emission spectroscopy or inductively coupled plasma-mass spectrometry on dissolved QDs. More extensive chemical information can be obtained from X-ray photoelectron spectroscopy or X-ray absorption spectroscopy (Supplementary Information 3). These structural and elemental data are complemented by optical spectroscopy, in which UV–Vis absorbance yields the QD band-edge transition and photoluminescence (PL) spectroscopy yields the emission wavelength, linewidth and PLQY, three of the figures of merit that are listed in Table 1.

Analysis of quantum dot core and surface

The quantum dot core. The characterization methods illustrated in Fig. 3 provide insight into QD quality needed for optimizing synthetic methods or application development but lack the precision required to construct realistic QD models. To obtain more detailed information on the geometry of the inorganic QD core, TEM is a preferred technique. Among the many TEM imaging modes (discussed in Supplementary Information 4), high-angle annular dark field-scanning TEM (HAADF-STEM) yields images in which intensity scales with the atomic number Z^n (Fig. 4a,b). In that way, the core and shell in heterostructures can be distinguished[59]. Moreover, in combination with spectroscopic techniques such as energy dispersive X-ray spectroscopy or electron energy loss spectroscopy, spatial composition maps of QDs can be obtained (Fig. 4c).

Although TEM can image QDs with atomic resolution, deriving the 3D structure of QDs from TEM images is not straightforward. Conventional TEM provides a 2D projection of a 3D object, which can be a poor representation of the actual geometry. Using TEM for 3D characterization is possible through electron tomography, a technique in which a series of projection images are acquired while tilting the sample over a range of angles that is as wide as possible[60]. However, QDs can suffer from considerable beam damage caused by exposure to high energy electrons during such time-consuming studies[61]. A less-demanding alternative is using advanced algorithms for 3D reconstruction to extract a 3D model of a QD from a single 2D projection[59]. This can be performed through a quantification of the image intensities in a STEM image, followed by molecular dynamics simulations[62] (Fig. 4d–g). The latter approach may be a route towards high-throughput characterization of QDs, eventually leading to an average structure, based on the characterization of many individual crystals.

A recent development to overcome electron beam damage is 4D STEM, a technique in which a full diffraction pattern is collected at each scan position[63]. Deviations of the centre of mass in these diffraction patterns are directly related to the electrostatic potential field, which results in an image intensity that depends linearly on the atomic number. Moreover, in 4D STEM, all electrons are collected by a hybrid pixelated direct electron detector, whereas in HAADF-STEM, only electrons scattered to relatively high angles are detected. Four-dimensional STEM can, therefore, be considered a very promising technique to resolve the atomic structure of QDs with limited electron beam damage. Alternatively, coherent diffractive imaging (CDI) is increasingly being used as a means to reconstruct atomistic structures of an object from the electron diffraction or XRD pattern[64,65]. CDI and time-dependent CDI might permit tomography and even movies of atomic motion as excitations displace atoms from equilibrium. Finally, an exciting outlook in the field of TEM is the possibility to perform experiments under the influence of specific triggers such as heat or light[66–68], in which dedicated sample holders enable investigation of QDs in a liquid environment. In this manner, the behaviour of QDs during application can be studied directly, which can lead to improved structure property connections.

The quantum dot surface. The initial methods for synthesizing colloidal QDs from metal–organic precursors used coordinating solvents, such as trioctylphosphine oxide, under the assumption that these moieties would impart colloidal stability by binding to the QD surface[4]. However, a detailed understanding of QD surface chemistry only emerged after years of in-depth chemical analysis. In particular, studies on CdSe QDs synthesized using cadmium carboxylates as the metal precursor showed that these QDs mostly carry no electric charge when dispersed in apolar media[69,70], have an excess of cations when compared with bulk CdSe[71,72] and bind two carboxylate ligands for each excess Cd^{2+} metal cation[73]. These observations demonstrated that QDs can be effectively seen as inorganic–organic hybrids, in which the properties of the inorganic core and the organic ligand shell are tightly interconnected. As outlined in Box 1, this insight inspired a classification of QDs based on the ligand binding motif, as described by the covalent-bond classification scheme[74]. For each of the resulting QD classes, charge neutrality is a guiding principle that relates the core and surface composition. In the case of CdSe QDs, for example, neutral L-type ligands – Lewis bases like primary amines – will cap stoichiometric QDs, whereas X-type oleates will terminate non-stoichiometric, Cd-rich QDs. Here, the net charge is to be calculated as the sum of the most stable oxidation states of all components.

NMR spectroscopy has been used to analyse QD surface chemistry. In ^{1}H solution NMR, ligands bound to QDs can be identified by their broadened resonances, small diffusion coefficients and negative cross peaks in a 2D nuclear Overhauser effect (nOe) spectrum[75] (Fig. 5a–c). Although the latter two are a result from the QD dictating the diffusion and tumbling behaviour of bound ligands, the ^{1}H NMR line broadening is more complex. Faster T_2 relaxation and heterogeneous broadening – demonstrated through spectral hole burning – indicate that both restricted motion and various local environments within the ligand shell contribute to the linewidth[76]. As a result, resonance linewidth is a sensitive probe of the ligand–solvent interaction, in which better solvation results in more narrow resonances[77]. Opposite from bound ligands, ligands in rapid exchange between a bound and free state will show narrow resonances with high diffusion coefficients, often indiscernible from the free ligand. However, such dynamic ligand binding can still lead to negative

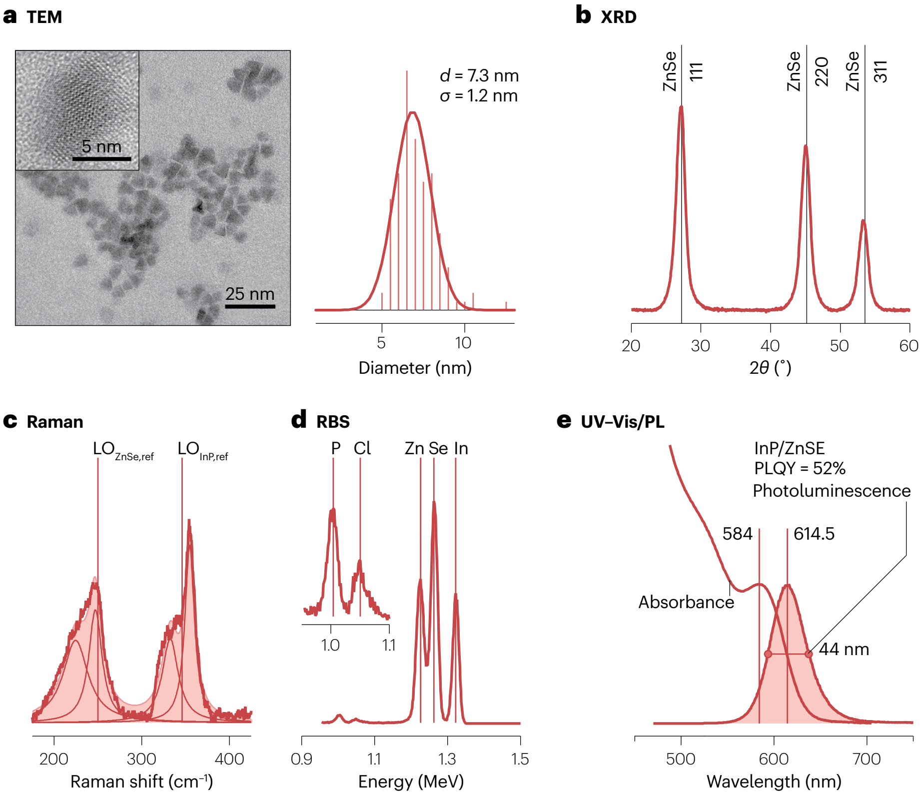

Fig. 3 | Typical characterization methods and results for InP/ZnSe quantum dots. a, Bright-field and high-resolution transmission electron microscopy (TEM) images provide an overview of the quantum dot (QD) size and crystallinity. Size analysis based on the overview image leads to the size histogram shown on the right. **b**, Powder X-ray diffraction (XRD) provides an indication of crystallinity at the ensemble level; in this case, the pattern is dominated by diffraction from the ZnSe shell. **c**, The Raman spectrum provides separate phonons of the InP core and the ZnSe shell; shifts with respect to reference wavenumbers are indicative of strain. **d**, Elemental composition can be derived from the Rutherford backscattering spectrum (RBS), in which the additional contribution from Cl is related to the QD surface. **e**, The ultraviolet (UV)–visible (Vis) and photoluminescence (PL) spectra provide an estimate of the band-edge transition – and therefore the QD size – as well as key figures of merit, such as emission wavelength, linewidth and photoluminescent quantum yields (PLQYs). Adapted with permission from ref. 56, American Chemical Society.

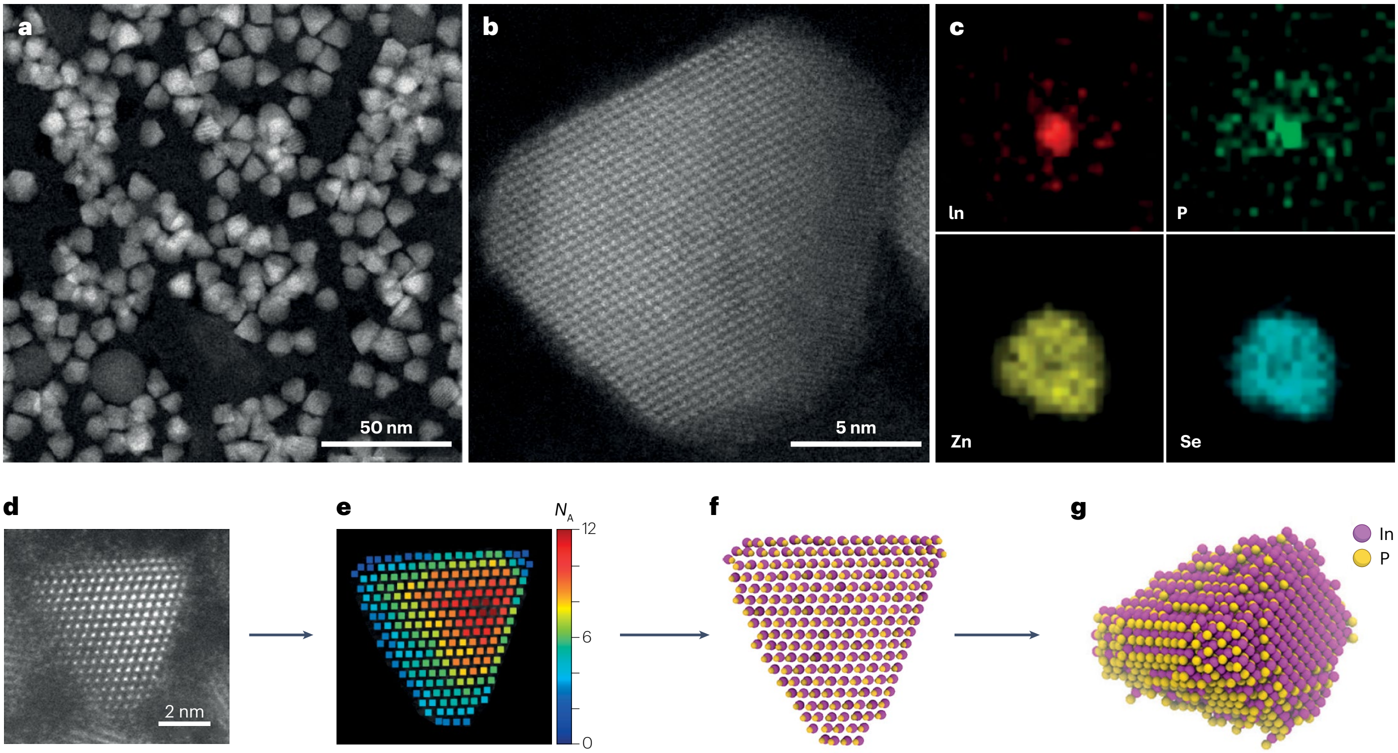

Fig. 4 | Chemical and structural characterization of quantum dots by electron microscopy and X-ray diffraction. High-angle annular dark field-scanning transmission electron microscopy (HAADF-STEM) images of InP/ZnSe core/shell quantum dots at low (part **a**) and high (part **b**) magnification. The high magnification depicts the ZnSe crystal along the [110] direction. Energy dispersive X-ray spectroscopy maps providing evidence for an InP core and a ZnSe shell (part **c**). Illustration on how a 3D model can be extracted by quantifying a 2D HAADF-STEM image (part **d**). Counts of the number of atoms (N_A) are indicated in part **e** and after structural relaxation a 3D model is obtained (parts **f** and **g**). Panels **a**–**c** adapted from ref. 286, ACS (https://doi.org/10.1021/acsphotonics.8b00615). Panels **d**–**g**, images courtesy of Kim Dümbgen (ref. 287).

nOe cross peaks, which makes the combination of 1D, diffusion-ordered spectroscopy and nOe spectroscopy NMR a powerful toolbox to analyse the QD ligand interaction[78] (Supplementary Information 5).

A limitation of ^{1}H solution NMR is the excessive line broadening of protons close to the QD surface owing to increasingly fast T_2 relaxation. Binding motifs are, therefore, often identified indirectly, through ligand exchange reactions, or by combining solution NMR with IR or solid-state NMR spectroscopy. Opposite from solution NMR, IR spectroscopy can probe the functional group by which ligands bind to the QD surface, a characteristic that is regularly used to distinguish, for example, carboxylic acids from carboxylates and identify specific binding modes[79]. Solid-state NMR, by contrast, can address a broad range of nuclei, including spin ½ nuclei such as ^{31}P, ^{77}Se or ^{113}Cd. Apart from identifying different chemical environments, cross polarization NMR spectroscopy provides insight into the coupling between the organic ligand shell and the inorganic QD core. In the future, such studies might benefit from the introduction of dynamic nuclear polarization enhancement, which cuts acquisition time and enables spectral features of different nuclei to be correlated[80].

Quantitative analysis of ligand binding. QDs in apolar media must remain charge-neutral; therefore, X-for-X and L-for-L exchanges are possible, whereas X-for-L or L-for-X are not (Box 1). Solution NMR can be used to monitor the titration of a QD dispersion with a new ligand, in which the resulting shift of the exchange equilibrium provides insight into the binding and packing of ligands. First developed for CdSe QDs, X-for-X titrations indicated that ligands do not form a homogeneous shell, but rather bind to specific facets[81]. An even more fruitful understanding was that, in the case of QDs classified as ME(MX$_n$), the entire MX$_n$ metal salt acts as a Z-type ligand – a Lewis acid – that can be displaced by the addition of L-type ligands, such as primary amines[82]. This L-type-driven Z-type displacement was linked to a dramatic loss of PL efficiency, whereas displacement isotherms, representing ligand coverage as a function of L-type ligand concentration, were used to survey the binding strength of, for example, cadmium oleate to CdSe and CdS[82–84]. Such studies showed a pronounced heterogeneity of binding sites at the QD surface, featuring stronger binding on specific facets and weaker binding on edges and corners; a conclusion confirmed by ab initio calculations of the site-dependent desorption energy[81] (Fig. 5d,e).

Computational analysis

Density functional theory. Determining the geometry, electronic energy levels and optoelectronic properties of a QD has been a central aim of the theoretical and computational analysis of QDs, and several methods are available for this purpose (Fig. 6a and Supplementary Information 6). Initial studies involved macroscopic models based on the effective-mass approximation[5], which provided analytical expressions for electronic energies, but reduced QDs to geometric shapes, such as spheres or ellipsoids[85]. Later, atomistic approaches, such as tight-binding and pseudopotential methods[86,87], led to more detailed insights into the relationship between the properties and the geometry of QDs. However, to recover bulk coordination and maintain overall charge neutrality, early atomistic methods were typically applied to unrelaxed QD models with surfaces terminated by pseudo-ligands; dummy atoms with scaled partial charges that passivate dangling bonds and preserve overall neutrality[85]. This approach inevitably neglected the impact of the QD surface on QD properties, a limitation that more recent computational studies overcome by applying first-principles methods such as density functional theory (DFT) to QDs. In DFT, QD surfaces need no passivation by pseudo-ligands and geometry optimization is possible without ad hoc parametrization. The result is a more comprehensive description, in which electron orbitals are obtained by considering both the QD core and the surface, eventually using a QD geometry that incorporates the actual surface ligands.

By using DFT from the outset, the challenge in describing QDs shifts to constructing QD models that accurately reflect their geometrical and chemical properties. QD models are, therefore, built according to the experimental QD composition and ligand binding motif (Fig. 6b). Model building is further supported by TEM imaging, which helps to identify the exposed crystal facets and may, eventually, provide an

Box 1 | Describing quantum dots as chemical compounds

Ligand classification

Given the boundary condition of charge neutrality, the quantum dot (QD)–ligand interaction can be conveniently described through binding motifs based on the covalent bond classification. As shown in the figure, this scheme discerns three types of ligands.

- L-type ligands: Lewis bases in their neutral form, contributing two electrons to the QD–ligand bond
- X-type ligands: compounds with an unpaired electron in their neutral form, contributing one electron to the QD–ligand bond
- Z-type ligands: Lewis acids in their neutral form, contributing no electrons to the QD–ligand bond

Often, X-type ligands will end up at the QD surface as anions that balance the charge of excess metal cations. Such ligands can also exhibit mixed character or even act in consort with another X-type ligand, forming a bound ion pair. For example, bound carboxylates could be classified as LX ligands, the additional L-type character arising from the carbonyl. Ion pairs often occur in reactions involving a mixture of amines and halide or carboxylic acids, forming ammonium halides or ammonium carboxylates. Such species can be labelled as XX′ or X_2 (ref. 291). The distinction between X or XX′ is important as it dictates how post processing ligand exchanges need to be optimized.

Binding motifs

Using the ligand classification, a QD can be written down as a chemical compound by combining the stoichiometric QD core with the ligand–QD binding motif. Writing a compound semiconductor as ME, in which the metal M has an oxidation state +*n*, examples include those listed in the table.

Binding motif	Description	Pictogram	Examples
$ME(MX_n)$	Cation-rich QD passivated by X-type ligands	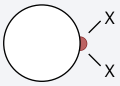	$CdSe(Cd(RCOO)_2)$[73], $PbS(Pb(RCOO)_2)$[28], $InP(In(RCOO)_3)$[79]
$ME(L)$	Stoichiometric QD passivated by L-type ligands	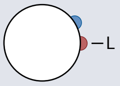	$CdSe(RNH_2)$[292]
$ME(MX_n)(L)$	Cation-rich QD with a mixed shell of X and L ligands. No definite X:L stoichiometry	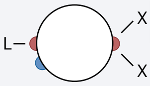	$InP(InCl_3)(RNH_2)$[293] $InAs(InCl_3)(RNH_2)$[294]
$ME(X_2)$	Stoichiometric QD with a mixed shell of positive and negative X-type ligands in a 1:1 stoichiometry	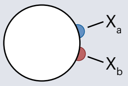	$CsPbBr_3(RCOO)(RNH_3)$[295] $CsPbBr_3(RCOO)(RNH_3)$[295] $HgSe(Cl)(RNH_3)$[296] $PbS(Cl)(RNH_3)$[297]

Ligand exchange reactions

Writing the QD–ligand construct as a chemical compound, ligand exchange processes can be expressed as chemical reactions that highlight the underlying breaking and formation of bonds. For example, exposing an $ME(MX_n)$ QD to an organic acid MX′ can lead to an X − X′ exchange according to:

$$ME(MX_n) + HX' \rightleftharpoons ME(MX_{n-1}X') + HX. \quad \text{(b1)}$$

Similarly, the displacement of an MX_n moiety by addition of L-type ligands can be expressed as:

$$ME(MX_n) + mL \rightleftharpoons ME(\bullet) + L_m - MX_n. \quad \text{(b2)}$$

Here, $L_m - MX_n$ is the resulting acid–base adduct.

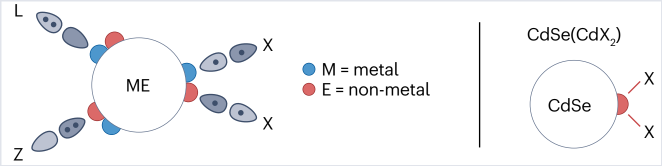

Figure adapted with permission from ref. 298, Royal Society of Chemistry.

A toolbox for surface chemistry analysis

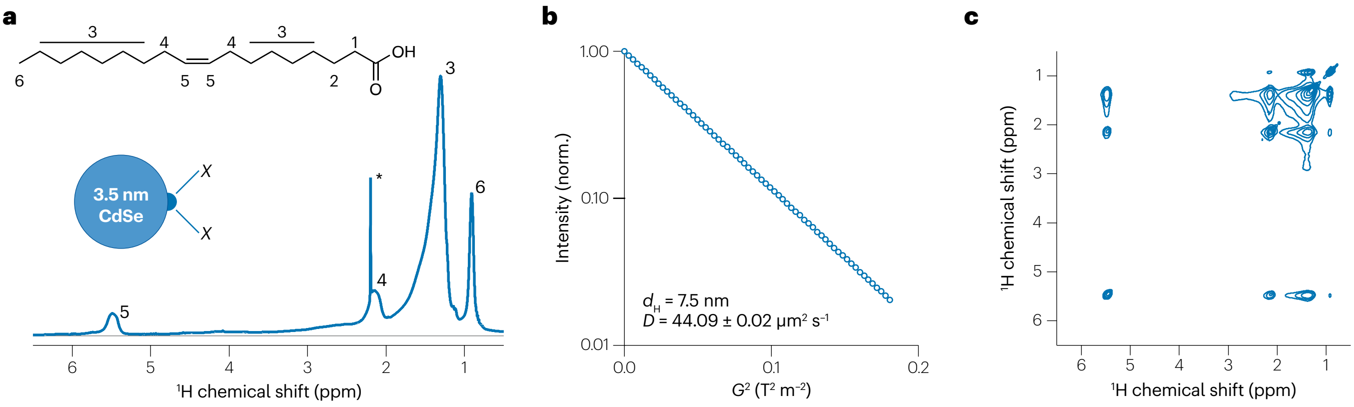

Leads to quantitative insight in QD–ligand binding

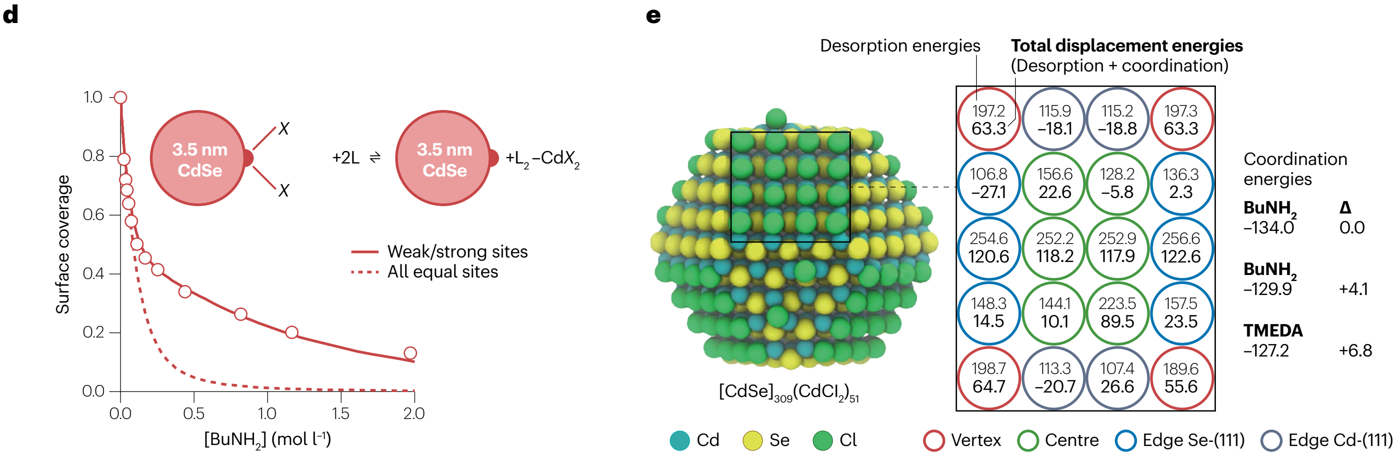

Fig. 5 | Quantum dot surface chemistry analysis. a–c, Illustration of the solution ^{1}H NMR toolbox applied to oleate-capped CdSe quantum dots (QDs), showing the 1D ^{1}H NMR spectrum with an identification of the resonances as indicated (part **a**), the intensity decay recorded through pulse field gradient spectroscopy, in which the slope of the intensity trace yields the diffusion coefficient (part **b**) and the nuclear Overhauser effect spectroscopy spectrum in which cross peaks with the same sign as the diagonal are indicative of species binding to the QD surface (part **c**). The NMR measurement was conducted in deuterated dichlorobenzene with a residual resonance indicated by the asterisk. **d**,**e**, Insight obtained from quantitative solution NMR studies; in this case, the surface coverage of CdSe QDs by cadmium oleate as a function of BuNH$_2$ concentration (part **d**), in which the agreement with an isotherm using two binding sites suggests a heterogeneity of binding sites confirmed by density functional theory calculations of the cadmium oleate displacement energy (part **e**). TMEDA, tetramethylethyldiamine. Parts **a**–**c** adapted from ref. 84, CC BY 4.0. Parts **d** and **e** adapted with permission from ref. 83, American Chemical Society.

atomically precise QD structure. In the absence of such detailed information, QD models can be set up using the Wulff construction, in which a given shape can be imposed by adjusting the surface energy of specific facets[88]. As QD facets can be abruptly terminated, it is essential to maintain charge balance by removing or adding atoms, while preserving the ligand-binding motif and the correct QD stoichiometry. Neglecting this aspect can lead to unintended artificial n-doping or p-doping, resulting in QD models that significantly deviate from real QDs. Once the QD model is established, the structure, including the surface, is allowed to relax, and the electronic structure is computed (Fig. 6b,c).

Relating geometry and electronic structure. A breakthrough in the study of QDs by DFT was the introduction of non-stoichiometric QD models, in which carboxylate ligands balanced the excess cadmium[89]. Building on this result, the impact of different ligand types on the QD electronic properties could be investigated[90]. In particular, the displacement of Z-type ligands was found to profoundly alter the electronic structure by creating two coordinated Se atoms that give rise to mid-gap states formed by localized, non-bonding Se 4*p* orbitals (Fig. 6c). The presence of these states, which act as surface traps, aligned with the experimental observation that Z-type displacement quenches the PL[82]. This discovery highlights that the interplay between a geometrical feature and an electronic feature — an undercoordinated surface atom yielding a trap state — impacts the competition between radiative and non-radiative processes and therefore the PLQY. These findings are broadly applicable, extending to larger QDs, other Z-type ligands and different II–VI and III–V QDs of various shapes[91–93].

The continuous improvement of computational architectures allows DFT computations on QDs 3–4 nm in size. Interestingly, DFT studies on such QDs yielded an energy separation between the highest

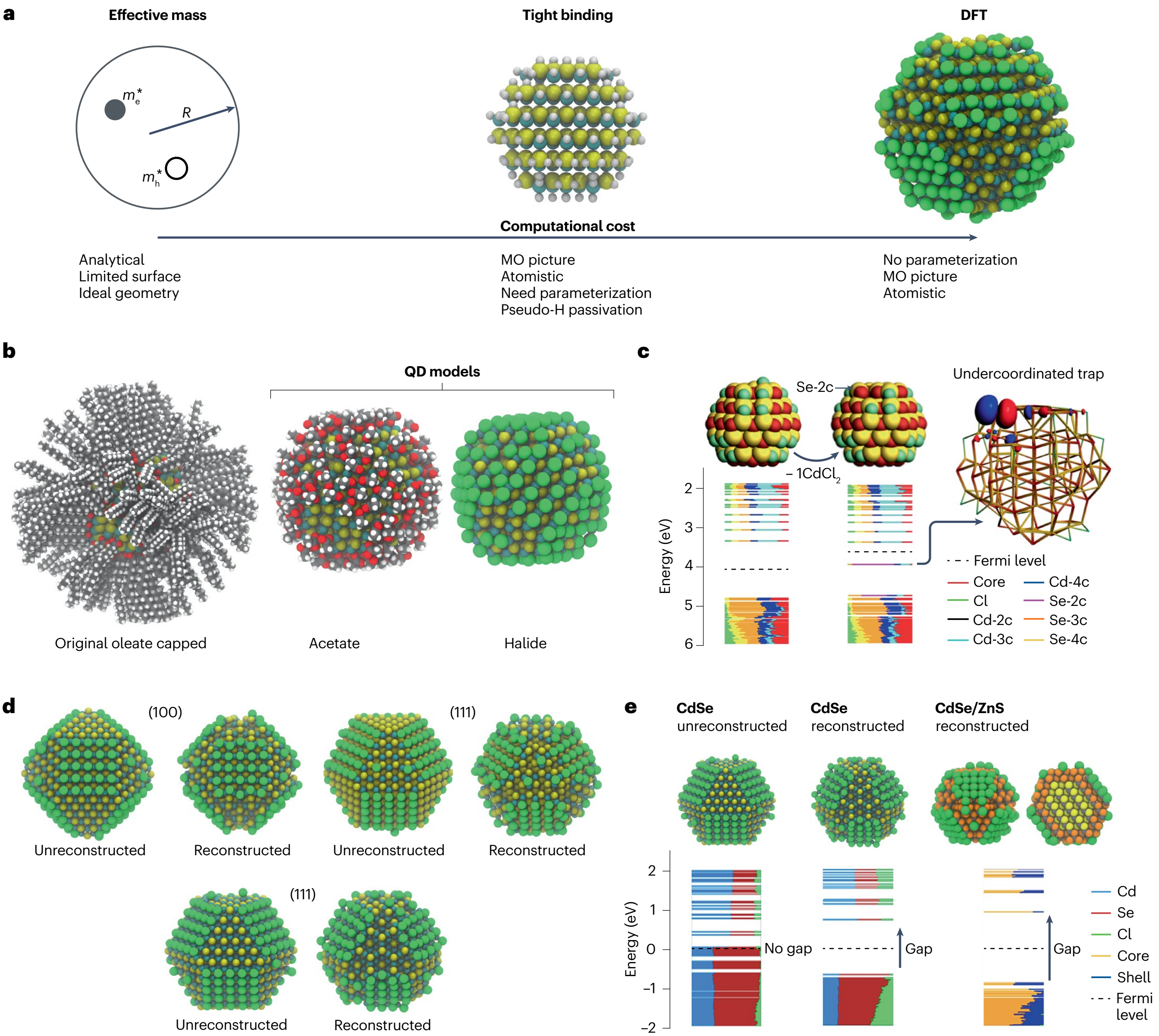

Fig. 6 | Computational analysis of quantum dots. a, Illustration of quantum dot (QD) modelling approaches and resulting information, comparing effective mass (analytical, ideal geometry), tight binding (molecular orbital (MO) picture, limited surface and needing parameterization) and density functional theory (DFT, atomistic, detailed surface and no parameterization), with an increasing computational cost from left to right. **b**, Schematic representation of an 'original' non-stoichiometric CdSe QD with a diameter of 3.5 nm, as synthesized, with its surface capped by oleate ligands. The QD models are atomistic representations of the original structure used in DFT calculations, in which the ligands are replaced with smaller moieties, such as acetate or halides. The excess charge of Cd in the inorganic core is compensated by the anionic ligands, resulting in a charge-balanced, neutral system. **c**, A view of a localized trap state, along with its density of states, arising from an undercoordinated Se atom in a CdSe QD model, following the detachment of a Z-type $CdCl_2$ ligand. **d**, Views from different zone axes of CdSe QDs, including a pure model with all facets fully passivated by Cd and Se ions, and a reconstructed CdSe QD model in which surface reconstruction patterns mitigate charge accumulation on ion-rich facets, specifically the 111 and −1−1−1 planes. **e**, Left: electronic structure of the unreconstructed CdSe QD model (3 nm in size), exhibiting a non-existent highest occupied molecular orbital–lowest unoccupied molecular orbital (HOMO–LUMO) gap owing to the presence of facet-specific trap states. Centre: the reconstructed CdSe QD model, built upon a vacancy pattern, showing the elimination of trap states and highlighting a clean HOMO–LUMO gap. Right: electronic structure of the surface-reconstructed core/shell CdSe@ZnS system, demonstrating a clean bandgap. Panel **c** adapted with permission from ref. 90, American Chemical Society. Panel **e** adapted from ref. 94, CC BY 4.0.

occupied molecular orbital and lowest unoccupied molecular orbital smaller than the bandgap of the same material in bulk, computed at the same level of theory[94]. Contradicting a basic characteristic of quantum confinement, this finding points towards an intrinsic issue in the construction of QD models. Typically, such models feature surface facets with the same geometry as bulk lattice planes. For bulk semiconductor surfaces, such facets are known to create surface states that can be eliminated by surface reconstructions. Such reconstructions follow specific patterns in which atoms can be expelled to form vacancies so as to suppress charge accumulation on the facet and the related surface states[95] (Fig. 6d). Interestingly, introducing such reconstructed facets in QD models yielded bandgaps consistent with expected values based on nanocrystal sizes (Fig. 6e). Importantly, this result enabled simulations of core/shell structures at the atomistic level, providing valuable insights into the energy-level alignment of core and shell components in systems that closely mirror experimental structures[96].

Time-resolved analysis

Time-resolved spectroscopy. As outlined in Supplementary Information 7, photo-excited QDs exhibit a range of competing relaxation pathways. Among these, radiative recombination and stimulated emission are widely used in light emission applications, whereas others are mostly seen as unwanted loss pathways. Preferred methods to analyse and quantify the relaxation of the photo-excited state are time-resolved PL (TRPL) and femtosecond pump–probe methods, such as transient absorption (TA). In TA, the change of the absorbance spectrum is probed with varying delays relative to an optical pulse with a typical time resolution of ~100 fs. In transient PL, the decaying emission intensity is recorded after pulsed excitation, with the most advanced set-ups offering picosecond or femtosecond time resolution.

Figure 7a–c summarizes a time-resolved spectroscopy study on $CsPbBr_3$ QDs[97]. TRPL at low-power excitation with nanosecond resolution gives access to the radiative recombination rate of single excitons, a QD figure-of-merit listed as the radiative lifetime $\tau_{X,\mathrm{rad}}$ in Table 2. At higher pump power, a short-lived, red-shifted emission band appears that is assigned to a biexciton population that quickly decays through Auger recombination. A complementary picture emerges from the TA map, which details the change in absorbance as a function of photon energy and delay time. Here, excitons occupying the band-edge states reduce or bleach the band-edge absorption, whereas biexcitons give rise to a short-lived band of stimulated emission (see Supplementary Information 6 for details). From the TA map, both energetic shifts and relaxation time constants of different photo-excited states can be deduced. Interestingly, the size-dependent electronic structure and interfacial or surface features of QDs fundamentally influence the energy and recombination rate of excited states, which offers inroads to design material responses to advance applications[98–103]. Here, a key result has been the increase of the biexciton Auger lifetime $\tau_{\mathrm{BX,Auger}}$ in CdSe/CdS QDs through the design of the core/shell structure[21,104] (Table 2).

Additional processes that can be tracked using time-resolved spectroscopy include intraband carrier cooling, carrier trapping, charge and energy transfer and exciton spin relaxation[98–103]. Means to understand thermalization of QDs and their surroundings can be important as heat dissipation processes may affect the long-term performance of QDs. Some studies have begun to investigate such questions with a focus on spectroscopies that target ligand thermalization after photo-excitation of QDs[105,106] or probe energy transfer across the semiconductor–organic interface by excitation of ligand vibrations[107].

Time-resolved diffraction for structural dynamics. Powder XRD is a widely used diffraction-based method to identify QD synthesis products. In addition, Scherrer broadening of diffraction peaks provides insight into average particle size (Fig. 7d) and single crystal diffraction and X-ray atomic pair distribution function analysis led to atomically precise structure models for magic-size clusters[108,109]. Combining static diffraction with in situ heating, early studies already revealed size-dependent melting temperatures that are reduced substantially from bulk owing to high surface energy[110], and related reports pointed towards ligand-induced and shell-induced surface strain[111]. By contrast, relaxation processes in excited QDs, such as charge-carrier cooling, non-radiative recombination and three-particle Auger recombination, impart energy to the lattice through phonons. As a result, QDs may sinter or even ripen; the QD lattice can distort, melt or undergo solid–solid transformations; the QD surface may reconstruct; and ligands may rearrange or detach[112,113]. In addition, the Coulomb field of photogenerated charges can locally distort the lattice. The resulting polarons lower the overall system energy and feature prominently in metal halide perovskite QDs[114].

Pulsed diffraction probes derived from synchrotrons and free electron laser X-ray sources[115–117], as well as kiloelectronvolt and megaelectronvolt pulsed electron sources[68,118–120], now offer means to monitor transient structural changes of the QD lattice. Similar to pump–probe spectroscopy, such experiments involve diffractive probing with a repetitious generation of non-equilibrium charge carriers, most commonly by pulsed photon absorption or electrical charge injection. Figure 7e illustrates how pump-induced changes in XRD signals relative to the unexcited sample give insights into structural changes. Lattice expansion, for example, leads to derivative-like difference signal, whereas phase changes and disordering result in a net loss of diffraction[121]. Figure 7f shows a graphical interpretation of data from Fig. 7e in terms of a solid–solid phase transition from orthorhombic to cubic symmetry.

From sub-ensembles to single quantum dots

The size and shape dispersion of QD ensembles can obscure detailed information regarding electronic density of states. Fluorescence line narrowing (FLN) experiments, such as those shown in Fig. 8a, circumvent this issue by using narrow-bandwidth, resonant excitation to selectively excite a lower-energy-absorbing sub-ensemble of QDs. This approach provided insight regarding the fine structure of the lowest-energy exciton states (Supplementary Information 7). FLN studies established the order and spacing of the bright and dark levels, phonon-assisted emissions (shifted by a phonon energy from a state), and emission from charged exciton states[122–124]. CdSe and InP QDs, for example, feature a lower-energy dark state and a higher-energy optically active bright state; an ordering that strongly increases the excited-state lifetime at low temperature, owing to reduced thermal access to the photon-coupled state[122,125,126]. Quantum confinement was found to strongly affect fine structure spacings, with dark–bright splitting up to tens of millielectronvolts for small QDs relative to a sub-millielectronvolt bulk value[127].

Unhampered by ensemble averaging, microPL (µPL) studies on single QDs showed crucial characteristics including spectral diffusion and fluorescence intermittency or blinking. As shown in Fig. 8b, periods of weak QD emission correlate with short excited-state lifetimes, which indicate that the low PLQY state may result from charged QDs that facilitate non-radiative Auger recombination. When Auger recombination can be suppressed, the PL intermittency is indeed greatly reduced, and lifetimes change less substantially even upon charging.

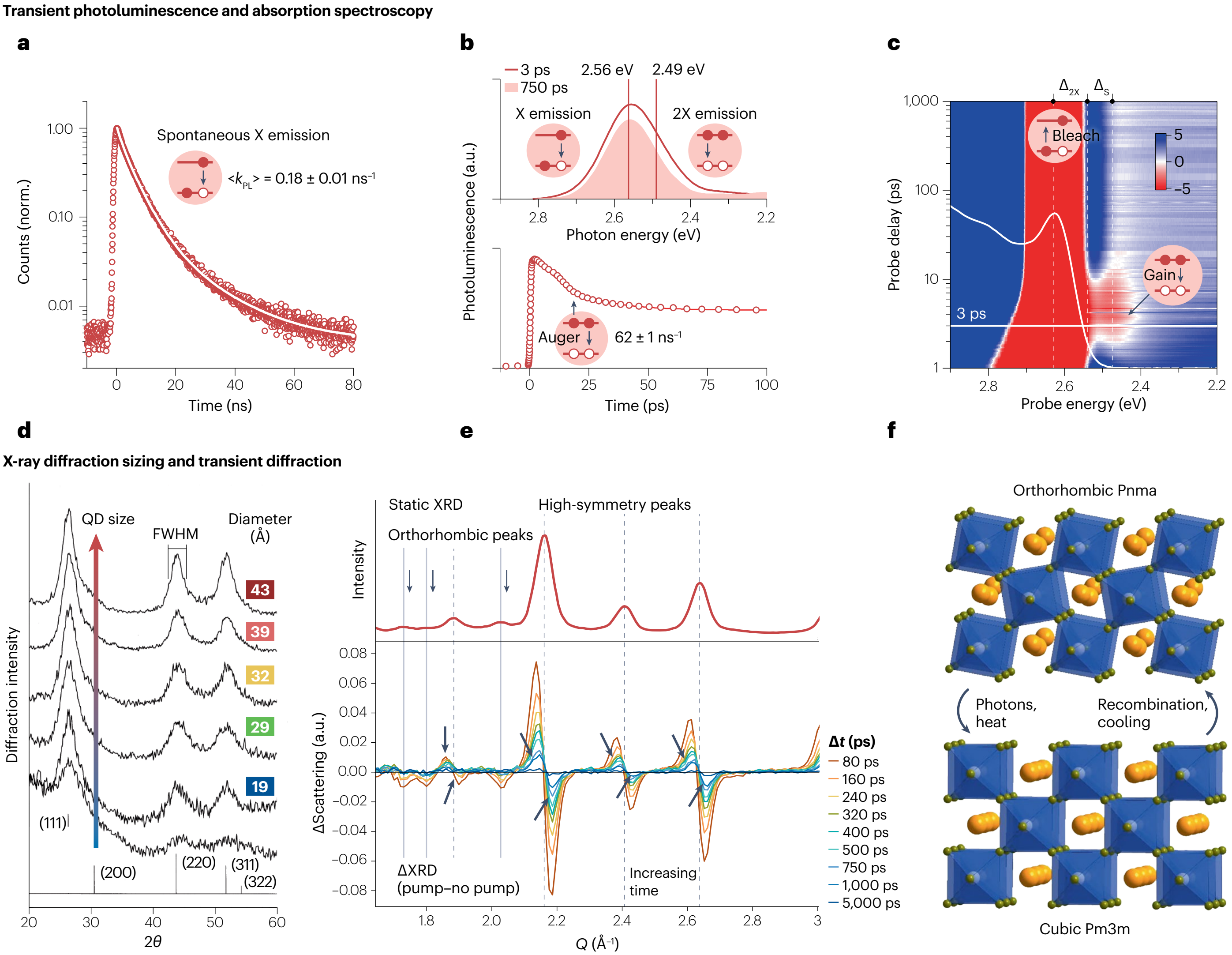

Fig. 7 | Time-resolved analysis of quantum dot properties. **a**–**c**, Transient optical spectroscopy analysis of 4.7 nm $CsPbBr_3$ quantum dots (QDs), including time-resolved photoluminescence spectroscopy with nanosecond (part **a**) and picosecond (part **b**) time resolution and femtosecond transient absorption spectroscopy (part **c**). The different decay components can be assigned to relaxation pathways of photo-excited QDs as indicated. **d**, Static X-ray diffraction (XRD) conveys lattice spacings and crystal symmetry. Full width at half maximum (FWHM) diffraction linewidths relate to average particle size. **e**, Transient X-ray diffraction static pattern (above) and pump-induced changes in the static pattern (below) for $CsPbBr_3$ QDs can relate expansion, disordering or phase transitions. Expansion appears as derivative line shapes with increased diffraction at low *Q* and reduced diffraction at higher *Q*, whereas loss of peaks can relate disordering, or in this case, in which diffraction is still observed for a cubic phase, convey a solid–solid phase transition (loss of peaks at grey vertical lines denoting orthorhombic peaks). **f**, Ambient temperature orthorhombic crystal phase with tilted octahedra converts to a cubic structure upon optical excitation that recovers to the initial state over time. a.u., arbitrary unit. Panels **a**–**c** adapted with permission from ref. 97, American Chemical Society. Panel **d** adapted with permission from ref. 288, American Chemical Society. Panels **e** and **f** adapted from ref. 121, CC BY 4.0.

Hence, unabated QD charging can deteriorate PLQY and, therefore, the efficiency of quantum LEDs (QLEDs); a finding highlighting the importance of rare ionization processes for fast, non-radiative relaxation, regardless of surface trap passivation[128–131]. The 2D maps of PL intensity versus excited-state lifetime (Fig. 8b, right-hand side) help to evaluate quenching mechanisms. For instance, neutral excitons emit slow with high intensity and three-particle Auger recombination active in charged dots reduces PL intensity and excited-state lifetime, whereas Auger-suppressed particles show higher brightness and longer lifetime than usual charged QDs. In addition, PL excitation spectroscopy on single QDs has been demonstrated, which helped to confirm electronic structure theory especially of hole states that can be challenging to characterize in QDs with a large hole effective mass and, consequently, a narrow energy spacing in the valence band[132]. Furthermore, fluorescence correlation spectroscopy has enabled analysis of single QDs in colloidal dispersion that offer insight into homogeneous PL linewidths[133]. Both FLN and μPL spectroscopies, including fluorescence correlation spectroscopy, have the potential

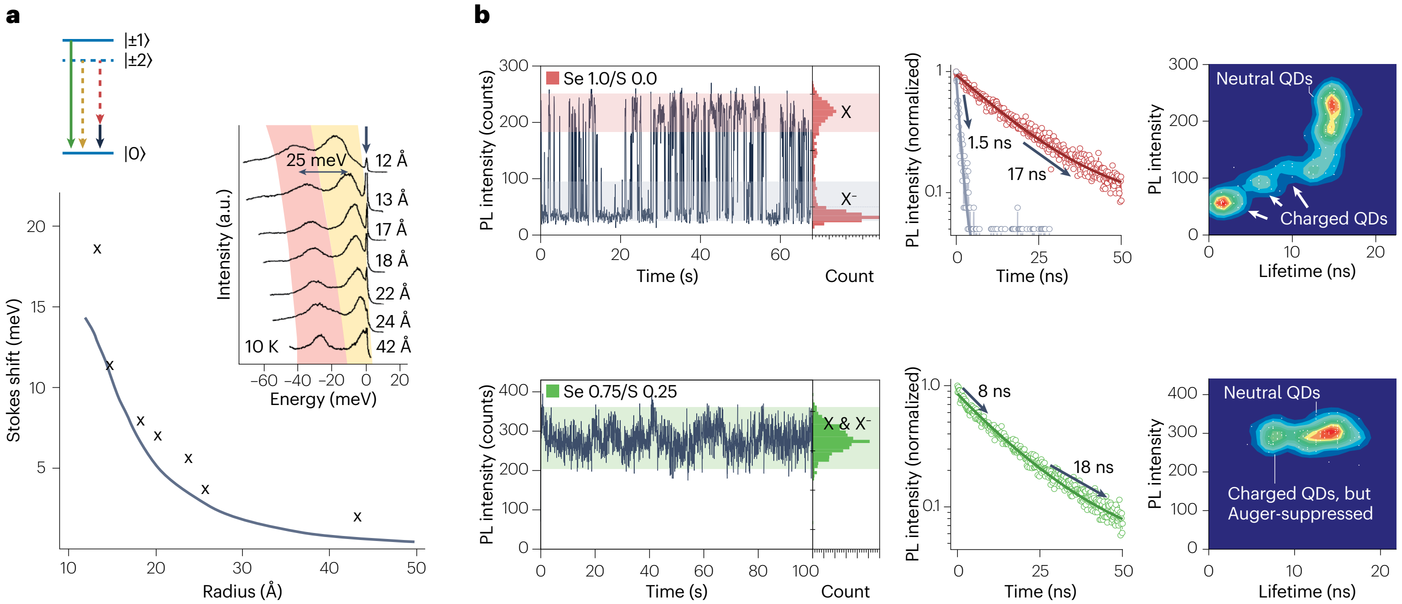

Fig. 8 | Spectroscopic study spanning sub-ensembles to single quantum dots. a, Using narrow linewidth optical excitation set to a wavelength close to the ensemble absorption onset (here for CdSe quantum dots (QDs)), light is absorbed only by a sub-ensemble of largest QDs in the ensemble with coupling into the optically active ±1 state that emits nearly at the same energy (green arrow). Spin relaxation to the optically passive dark state yields a Stokes shifted emission (orange dashed arrow and orange shaded region). A still redder emission arises from local oscillator phonon assistance from the optically passive state (red dashed arrow and red shaded region). Such fluorescence line narrowing spectra (inset) result for indicated QD sizes and reveal a size-dependent spectral shift from optically active to passive state, revealing dark–bright splitting size dependence. **b**, For spatially isolated single QD investigations, photoluminescence (PL) intermittency or blinking is shown in the upper row in which measured lifetime decreases markedly when PL count rates drop (evaluated by time-tagging each photon arrival time). The lower row shows a particle with suppressed blinking and a reduced distribution of emission lifetimes. Excited-state lifetimes show rapid emission for typical QDs that undergo non-radiative Auger recombination, whereas certain core/shell particles, although they occasionally still charge, can still radiate as the Auger process is suppressed and indeed emit with a shorter lifetime owing to the additional charge. a.u., arbitrary unit. Panel **a** adapted with permission from ref. 122, American Physical Society. Panel **b** adapted with permission from ref. 289, American Chemical Society.

to become especially insightful if eventually possible to combine with atomic-resolution methods such as STEM or X-ray tomography.

Charge transport in quantum dot films

Mobility. Many applications of QDs require the transport of electrons and holes between QDs in solid films, which take place via drift or diffusion of charge carriers. These processes are governed by the density (n), lifetime (τ) and mobility (μ) of the charge carriers, which is defined as the ratio between the speed of charge carriers and the applied electric field. The requirements on these parameters strongly depend on the application. QD LEDs contain a few layers of QDs at the most, wherein electrons and holes are injected directly from contacts. Here, a high mobility is not required. Photodiodes operate at reverse bias (V_R) where most transport occurs via drift. The minimum mobility (μ_{min}) is set by the requirement to extract charge carriers from the absorber layer with thickness (x) faster than the carrier lifetime, such that $\mu > x^2/\tau V_R$. For a 200 nm thick QD film at 2 V reverse bias and a carrier lifetime of 2 ns (refs. 134,135), one thus obtains μ_{min} = 0.02 cm^2 V^{-1} s^{-1}. Solar cells usually rely on the extraction of carriers via diffusion. In that case, the minimum mobility is determined by the requirement that the carrier diffusion length L_D exceeds the film thickness, such that $L_D = \sqrt{D\tau} > x$ and thus $\mu > x^2 e/\tau k_B T$. Using the same numbers as before, one finds $\mu_{min} = 1.6 \mathrm{cm}^2/\mathrm{V}^{-1}\mathrm{s}^{-1}$. High-speed photodetectors (PDs) and transistors would require even higher mobilities.

The hopping limit. In QD films, long-range charge transport is limited by the rate at which carriers hop from QD to QD. Hopping involves a transfer of charge from an initial to a final orbital on adjacent QDs whose energy is temporarily aligned through thermal activation (Fig. 9a). The rate constant k_{ET} for hopping can then be described with the Marcus equation:

$$k_{ET} = \frac{2\pi}{\hbar} J^2 \frac{1}{\sqrt{4\pi\lambda k_B T}} \exp\left(-\frac{(\Delta G^o + \lambda)^2}{4\pi\lambda k_B T}\right). \qquad (2)$$

Here λ is the reorganization energy, ΔG^o is the free energy difference and J is the electronic coupling between the adjacent QD orbitals. For weak coupling, J can be approximated by a tunnelling term, in which lower and shorter barriers lead to larger coupling. For identical QDs, ΔG^o is 0, and the activation energy amounts to $\lambda/4$. Size dispersion results in a distribution of the HOMO and LUMO energies, and differences in ligand packing or the surrounding electrostatic environment further shift the energy levels, increasing ΔG^o. The reorganization energy λ is usually dominated by polarization of the environment owing to charge transfer and is, in that case, equivalent to the solvent reorganization term λ_0 in the Marcus theory[136]. In the hopping or weak coupling limit, the mobility is proportional to k_{ET}:

$$\mu = \frac{(2r+d)^2}{6k_BT}k_{ET}. \tag{3}$$

Here, r is the QD radius and d the QD interdistance. Hence, a lower reorganization energy, a smaller spread in site energies or increased electronic coupling will enhance mobility.

Band-like transport. Stronger coupling gives rise to mini-bands with a width $W = 4J$, which results in a broadening of optical features and a decrease in the bandgap[137] (Fig. 9b). The limit of strong coupling is formed by bulk semiconductors, in which W equals the width of the conduction or valence band (Fig. 9c). When W exceeds the spread in site energies and the activation energy, electrons can delocalize across multiple QDs. In this case, scattering with lattice phonons, ionized impurities or other charge carriers results in a mobility $\mu = e\tau/m^*$, proportional to the scattering time τ and inversely proportional to the effective mass (m^*). Opposite from hopping transport, the mobility in the band-like transport regime reduces with increasing temperature owing to more effective phonon scattering. Temperature deactivation of the mobility is, therefore, often seen as evidence for band-like transport[138–140].

The mobility spectrum. The exchange of the as-synthesized long ligands by short organic or inorganic moieties has been used to enhance the mobility in QD films by orders of magnitude, reaching the required limits for device applications (Supplementary Information 8). Such films are not characterized by a single mobility; rather, mobility depends on the charge-carrier density and frequency at which carrier motion is probed. In QD films, disorder in size, electronic coupling, electrostatic environment and the presence of shallow defects create a spread in energy levels, which increases the activation energy for hopping (Fig. 9a). A higher orbital occupation, for example, related to doping, photo-excitation or gating, decreases the average activation energy and thus increases the measured mobility. The highest charge densities are achieved in electrochemically gated transistors[141,142], followed by field-effect transistors[143]. Photoconductivity and Hall measurements usually operate at low occupation[141,142]. Furthermore, domains of strongly coupled QDs are often separated by regions with weaker coupling (grain boundaries). The mobility within a single domain can be high, whereas the long-range mobility is limited by the grain boundaries. Therefore, mobility measured in a transistor geometry will depend on the distance between the source and drain electrodes. Contactless measurements such as time-resolved microwave conductivity or terahertz conductivity probe charge transport by measuring the absorption of gigahertz or terahertz radiation by free carriers[138]. Within half a period of the ac field, the carriers only probe a small volume of the sample and are much less sensitive to long-range disorder. The fact that the measured terahertz or gigahertz mobility is often higher than the reported dc mobilities reflects the fact that mobility is a spectrum, not a number.

Applications

QDs offer significant potential for integration in diverse technologies owing to their widely tunable optoelectronic and chemical properties. Examples include thermoelectrics[144]; non-volatile memories[145]; solar energy harvesting[13,146–148]; optoelectronics, ranging from colour conversion in displays and lighting to electroluminescent diodes and image sensors[149,150]; and quantum photonics[151]. However, as-synthesized QDs are often ill-suited for these applications. The capping of insulating organic ligands prevents charge transfer to and from QDs and can be incompatible with preferred solvents or an envisaged polymer matrix. QD applications, therefore, typically start with ligand exchange, which is nowadays mostly part of an initial QD ink formulation process (Supplementary Information 8). By means of such inks, QDs are processed into densely packed thin films using versatile wet-deposition techniques such as spin coating, spray coating and dip coating and scalable methods such as inkjet, roll-to-roll and transfer printing.

Luminescent colour convertors are typically made by dispersing QDs in a polymer encapsulant[152], whereas optoelectronic devices are formed by integrating QD films in multilayer stacks. Fabrication methods include metal thermal evaporation, atomic layer deposition

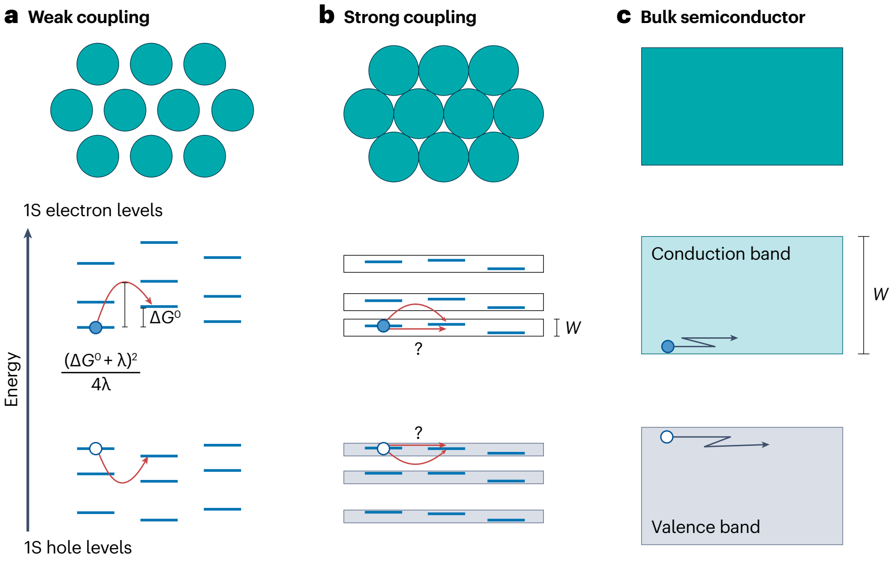

Fig. 9 | Charge transport limits in quantum dot films. Weak coupling (part **a**) leads to hopping transport, whereas strong coupling results in mini-band formation (part **b**) and may result in band-like transport, like in bulk semiconductors (part **c**), in which the mobility is limited by charge-carrier scattering.

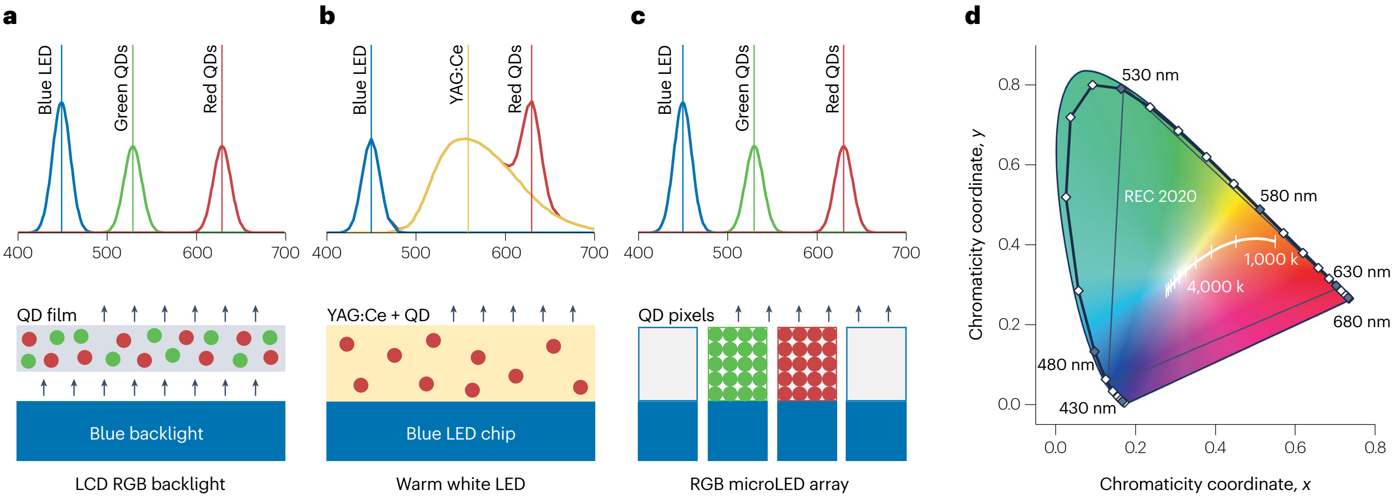

Fig. 10 | Colloidal quantum dot colour conversion. Working principle of quantum dot (QD) colour conversion for liquid crystal display (LCD) backlights (part **a**), warm white light-emitting diodes (LEDs) (part **b**) and blue microLED arrays (part **c**), showing schematically the integration of QDs in the device (bottom) and the resulting emission spectrum (top). **d**, Chromaticity diagram showing a locus of colour points accessible to QDs with an emission linewidth of 20 nm. The light grey line represents the REC 2020 standard for RGB displays (International Telecommunications Union (ITU) Recommendation BT 2020). The while line represents the Planckian locus used to assign a colour temperature to white light emitters.

and sputtering techniques. By adjusting the device architecture, such stacks can function not only as LEDs and PDs but also as QD solar cells, lasers or transistors. Interestingly, several studies showed that these fabrication steps can be replaced by a printed equivalent, leading to fully printed QD optoelectronics[153]. Opposite from such dense QD films, which easily contain trillions of QDs per square centimetres, applications in quantum technology require single QDs. Although proof-of-principle studies can make use of random deposition, even within the gap separating two gold electrodes, deterministic deposition of single QDs on substrates remains an outstanding challenge.

Quantum-dot-based colour converters

With a narrow emission and a broad excitation spectrum, QDs are nearly ideal fluorophores for spectrum-on-demand light sources based on luminescent colour conversion. As shown in Fig. 10, the partial conversion of the blue light of an InGaN LED into nearly monochromatic red and green emission lines by QDs has been used to create a backlight for liquid crystal displays that gives access to a much broader colour gamut than the spectral filtering of white light[154,155] (Fig. 10a), realize white LEDs in which the addition of a narrow red QD emission to prevailing powder phosphors, such as YAG:cerium, improves colour rendering and reduces the colour temperature without wasted IR emission[156] (Fig. 10b) and form microLED displays, in which red and green primary colours are formed through QD-on-chip colour conversion starting from a single blue microLED pixel array[157] (Fig. 10c). Furthermore, the same principle of colour conversion by QDs has been implemented in LSCs, in which QDs embedded within a window pane re-emit absorbed sunlight towards solar cells mounted at the pane edges[10].

In liquid crystal displays, a QD-in-polymer film is typically inserted within the optical stack that diffuses and filters the backlight[158]. Through this remote phosphor approach, QDs are exposed to relatively low optical power – typically 0.1 $\mathrm{W\,cm^{-2}}$ – and encapsulation methods can mitigate possible photodegradation issues. QD-on-chip colour conversion – preferred for lighting and miniLED/microLED displays – involves significantly higher optical power levels – 10–100 $\mathrm{W\,cm^{-2}}$ – and operation temperatures of 100 °C or more. Although QDs deteriorate more quickly under such conditions, warm white LEDs with excellent colour rendering and a luminous efficacy as high as 170 $\mathrm{lm\,W^{-1}}$ were demonstrated using Cd-based and InP-based QDs[159,160]. Furthermore, turning a blue pump light into a single, monochromatic light source was achieved using InP/ZnSe/ZnS QDs with near-unity PLQY on-chip[8].

Ideally, QDs for colour conversion feature a high absorption coefficient at the pump wavelength, a narrow, broadly tunable and fast PL with a near-unity PLQY, irrespective of temperature, and minimal spectral overlap between absorption and emission. Strong light absorption minimizes the amount of QDs needed and is key to fully absorb blue light across films a few micrometres thick in QD-on-chip microLEDs. Narrow and broadly tunable emitters offer the widest colour gamut for displays, as shown in the chromaticity diagram in Fig. 10d, and enable a desired emission spectrum to be precisely reproduced. A near-unity PLQY maximizes conversion efficiency, and a short radiative lifetime avoids saturation at high pump powers. Minimal spectral overlap is essential to avoid self-absorption, which exacerbates conversion losses unless the PLQY is 100%. According to Table 1, CdSe/CdS QDs stand out for blue-to-red colour conversion. In particular, as the CdS shell strongly absorbs blue light, self-absorption can be suppressed by increasing the shell volume. $CsPbBr_3$ QDs are even more narrow emitters, feature a similar absorption coefficient for blue light but offer little tunability of the absorption coefficient at the emission wavelength. The most widely used colour converters, however, are InP/ZnSe or InP/ZnS QDs, which are free of restricted elements such as Pb or Cd. Even so, as only the InP core effectively absorbs blue pump light, using these to make QD-on-chip microLEDs remains challenging.

Quantum-dot-based printed optoelectronics

Quantum dot photodetectors. QD films have been integrated as the photosensitive layer in photoconductors, phototransistors and photodiodes (see Supplementary Information 9 for details on fabrication methods). QD PDs (QDPDs) stand out by their capability of detecting short-wave IR (SWIR) and mid-wave IR light. However, to fully lever the distinctive potential of QDs in this field, it is critical to link the QD electronic properties, the inner physics of the device comprising the QD film and other layers and the consequent device characteristics[13,148].

For QDPDs in a photodiode architecture, photon absorption is accompanied by generation of excitons within the QD layer. These bound electron–hole pairs dissociate into free carriers, which are transported through the charge transport layers (CTLs) to the metal electrodes, where they are collected as photocurrent (Fig. 11a). In terms of characterization, the initial steps of photon absorption and exciton generation are analysed using optical techniques such as absorption spectroscopy, PL, TRPL, external quantum efficiency (EQE) and TA (Figs. 3 and 7). Band alignment can be derived through UV photoelectron spectroscopy (Supplementary Information 3). Charge-carrier dynamics, encompassing both transport and recombination processes, are evaluated through methods such as electroluminescence, transient photocurrent and photovoltage, intensity-dependent photocurrent and voltage-bias-dependent EQE measurements. Charge extraction at the interfaces with CTLs and electrodes, in turn, is critically assessed using techniques such as space-charge-limited current, impedance spectroscopy, charge extraction by linearly increasing voltage and transient electroluminescence. Collectively, these techniques provide a framework for elucidating the interplay between single photophysical processes and overall device performance.

Different electro-optical probing techniques, complemented by spectral analysis, are used to characterize the performance parameters of QDPDs. Wavelength-dependent responsivity, EQE and detectivity

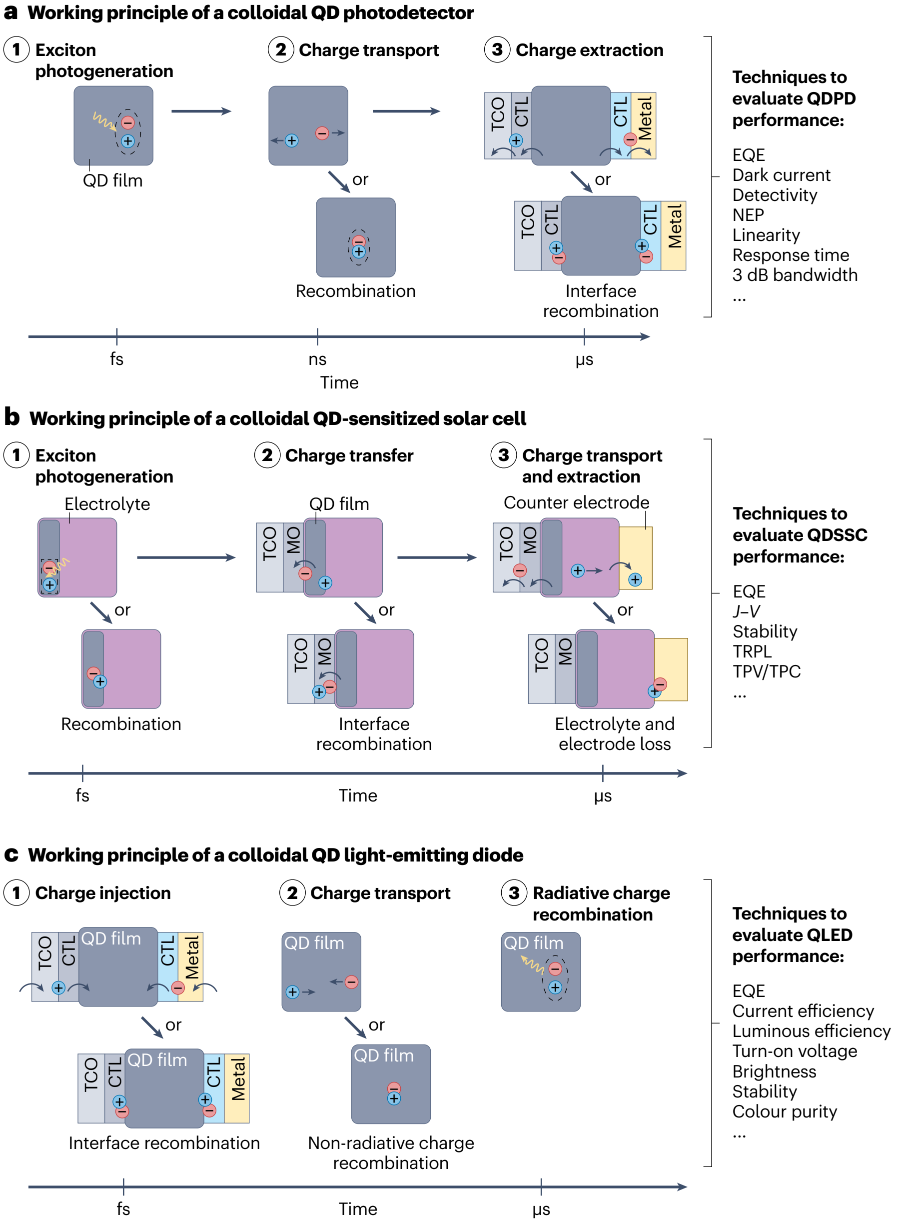

Fig. 11 | Colloidal QD-based photodetectors, QD-sensitized solar cells and QD light-emitting diodes working principles and performance limiters explored via electro-optical characterization techniques. Key processes in quantum dot (QD) photodetectors (QDPDs) (part **a**), QD-sensitized solar cells (QDSSCs) (part **b**) and QD light-emitting diodes (QLEDs) (part **c**) occurring across different timescales, along with selected experimental techniques for probing the corresponding device performances. CTL, charge transport layer; EQE, external quantum efficiency; MO, metal oxide; NEP, noise equivalent power; TCO, transparent conductive oxide; TPC, transient photocurrent; TPV, transient photovoltage; TRPL, time-resolved photoluminescence.

quantify the light absorption capabilities and light response of QDPDs. As a function of the QD bandgap, QDPDs can be classified into three categories: wide-bandgap UV (such as graphene, ZnO and ZnSe QDs), Vis (such as CdS, CdSe and perovskite colloidal QDs) and narrow-bandgap IR PDs (such as InAs, PbS and HgTe colloidal QDs). Depending on the device geometry and operating mode, responsivities ranging from 10^6 A W^{-1} to 10^9 A W^{-1} across the UV-to-IR spectral window have been reported, with phototransistors currently exhibiting superior performance compared with their photodiode (10–10^5 A W^{-1}) and photoconductor (10^{-4}–10^3 A W^{-1}) counterparts[135,149]. Furthermore, detectivities of 10^{18} Jones in the UV range and roughly 10^{12} Jones for wavelengths greater than 1.8 μm have been achieved across various device geometries[135,149].

Characterizing the response speed of a PD, the 3 dB cut-off frequency depends on the carrier lifetime and the RC time constant of the PD circuit. It quantifies the ability of the QDPD to respond to modulated light across different frequencies. Transient photocurrent and TA are commonly used to assess the temporal response, including fall and rise times. These measurements provide valuable insights into charge-carrier dynamics, encompassing parameters such as carrier mobility, lifetime and trapping–de-trapping processes. Response times as fast as a few nanoseconds, if not even lower, are reported for QDPDs targeting the SWIR and Vis–NIR spectral regime[135,161].

Quantum dot-sensitized solar cells. Colloidal QDs have been incorporated into photovoltaic solar cells primarily as light-absorbing sensitizers in QD-sensitized solar cells (QDSSC) and as the light-absorbing layer in QD solar cells and QD heterojunctions. The tunability of the bandgap and light absorption properties, coupled with the potential for flexible and low-cost fabrication, positions QD-based solar cells as a promising area for innovation and the advancement of future solar energy technologies.

A QDSSC consists of three primary components: a QD-sensitized photoanode, a counter electrode and an electrolyte containing a redox couple. The photoanode is typically composed of nanostructured metal oxides, such as ZnO, SnO_2 or TiO_2, coated with fluorine-doped tin oxide or indium tin oxide. The selection of QDs for sensitization depends on the desired optical and electronic properties, with widely used materials including CdS, CdSe, CdTe, InAs, PbS and $CuInS_2$ (refs. 162,163). Various synthesis and sensitization techniques are used for QDs, including chemical bath deposition, successive ionic layer adsorption and reaction, solution-based hydrothermal synthesis, hot-injection colloidal synthesis and direct adsorption. The key differences among these methods are primarily associated with their effectiveness in controlling nanoparticle agglomeration, spatial distribution, precursor utilization efficiency, processing time and resource requirement and overall scalability. The electrolyte, generally based on sulfide–polysulfide or iodide–triiodide redox couples in a liquid or quasi-solid state, is positioned between the photoanode and the counter electrode, which is often composed of Pt or Cu_2S.

The operation of a QDSSC can be sequenced into four processes as shown in Fig. 11b. First, photon absorption and subsequent exciton generation occurs within the QDs. Then, electrons are transferred from the QDs to the metal oxide and the oxidized QDs are regenerated via electron donation from the redox electrolyte. Finally, redox regeneration occurs at the counter electrode. Similar to colloidal QD photovoltaics, the initial light absorption and exciton generation can be analysed using optical techniques such as absorption spectroscopy, PL and TRPL. For charge transport characterization and carrier lifetime measurements, transient techniques such as TRPL, photoconductance decay, short-circuit current decay and open-circuit voltage decay are commonly used[164]. The regeneration of oxidized QDs is typically investigated using a combination of electrochemical impedance spectroscopy, surface photovoltage spectroscopy, open-circuit voltage decay and TA. The redox regeneration process at the counter electrode, which has a crucial role in sustaining continuous charge flow, is studied using techniques that focus on catalytic activity, charge transfer dynamics and interfacial electrochemistry. The most relevant methods for this purpose include electrochemical impedance spectroscopy, chronoamperometry, Raman spectroscopy and Fourier-transform IR spectroscopy.

The overall photovoltaic performance of a QDSSC is ultimately evaluated through standard current–voltage (J–V) measurements, which yield key performance parameters, including the fill factor, open-circuit voltage (V_{oc}), short-circuit current (J_{sc}) and power conversion efficiency. In state-of-the-art QDSSCs, the power conversion efficiency has surpassed 15%, with recent advancements achieving values exceeding 17%[165–167]. In the coming years, research on QDSSCs should focus on minimizing charge recombination losses, enhancing QD material stability and improving the efficiency of charge transfer processes. This includes advancing interface engineering and optimizing counter electrode materials. Further development of synthesis techniques, doping processes and substrate treatments will also be essential for improving device performance and achieving commercial viability.

Quantum dot light-emitting diodes. QLEDs make use of a diode architecture optimized to inject charge carriers into a QD film. QLEDs constitute monochromatic light sources that can seamlessly cover the full visible spectrum. QLEDs rely upon the injection of charge carriers from the metal electrodes into the adjacent CTLs. These carriers are transported through the CTLs and the QD emissive layer recombining radiatively and thus emitting light at a wavelength determined by the QD size (Fig. 11c). Notably, each of these steps – charge injection, transport and recombination – occurs at distinct spatial locations within the QLED device and on different timescales. Charge injection is analysed using techniques such as current–voltage (I–V) measurements, impedance spectroscopy and electroluminescence; charge transport dynamics are often probed through space-charge-limited current measurements and charge extraction by linearly increasing voltage. The radiative recombination processes in the QD film can be investigated via EL, EQE, transient electroluminescence and thermally stimulated luminescence measurements.

QLEDs emitting visible light are broadly categorized based on the primary emission colour as blue, green and red. For each of these categories, QDs with PLQYs above 95% and, in some cases, reaching unity are available (Table 1). The electrical device characteristics and temporal response are assessed using turn-on voltage and fall/rise time[168,169], reporting on charge transport dynamics, carrier recombination and device efficiency. Full assessment of optical performance relies on spectral analysis, luminance and radiant flux measurements in combination with electrical characterization, as well as imaging and spatial analysis. Key parameters include the luminous efficacy, EQE and colour rendering index, which collectively provide a comprehensive picture of light output and colour quality. The EQE is critical for understanding the efficiency with which electrical energy is converted into light, whereas luminous efficacy measures the effectiveness of the LED in producing visible light as perceived by the human eye. To date, EQEs of QLEDs have reached 20%[14,168], with some devices even exceeding 25% and approaching, if not even surpassing, 30%[170,171]. Notably, there is a significant discrepancy in stability among different colours of QLEDs. Red QLEDs exhibit superior longevity, with a $T_{50} > 10^6$ h at 100 nits, currently outperforming their blue and green counterparts[14]. Enhanced understanding of these parameters is essential for advancing QLED technologies, particularly in applications requiring high colour accuracy and luminous output, such as display technologies, general illumination and automotive lighting systems.

QDPDs and QLEDs thus share a set of common performance constraints, including poor charge transport and electric field distribution, losses owing to inadvertent recombination, incomplete surface passivation, insufficient light absorption and inefficient charge collection or injection. These limitations are intrinsically linked to the physical and structural properties of the QD-based optoelectronic device, as well as the material characteristics of the QDs. Examples of these properties include charge-carrier mobility, QD size and shape, QD surface defect density and interface quality.

Quantum optics

Although atoms have been traditionally at the heart of quantum optics[172], QDs are emerging as a viable, solid-state alternative. This evolution is spear-headed by the technological developments with epitaxially grown III–V QDs[173]. Even so, colloidal QDs have been penetrating more and more into these domains recently, even if QD-based quantum optics faces considerable challenges[174,175] (Supplementary Information 10). Most mature are single-photon sources, which are a central component for quantum communication[176], photonic quantum computing schemes[177] and quantum sensing[176]. Existing commercial products are based on epitaxial QDs. Although limited to a narrow wavelength range and in need of deep cryogenic cooling, epitaxial QDs offer a benchmark for colloidal QDs, which promise a wide spectral tunability and easier fabrication but need better stability, photon quality (indistinguishability and purity) and efficiency before commercial applications become viable. An important advance, that up to now is only fully exploited with epitaxial QDs, is integration into optical microcavities that allow to boost the performance of single-photon sources[178] and enable effective photon–photon interactions to be realized in the strong light–matter coupling regime[179]. Beyond single QD devices, collective effects may be used to generate multipartite entangled states that could become a useful resource for both quantum computing and sensing applications. Cooperative emission from several emitters currently appears challenging with epitaxial QDs, whereas there has been promising, initial demonstrations with colloidal QDs. By contrast, entanglement and efficient extraction of the correlated photons still need to be established.

Single-photon sources. Stable emission, both spectrally and by intensity, is essential to even consider a QD as a source of single photons[180,181]. This can be determined for individual QDs using μPL[182]. Resonant excitation with detection of the phonon replica[183] and photon-correlation Fourier spectroscopy[184] can give access to fluctuation timescales below the millisecond regime, and some techniques can even extract such information from ensembles[185]. Refining synthesis, structure and composition can help to reduce detrimental effects such as charge fluctuations and traps. With colloidal II–VI QDs, the growth of thick or graded multishells tremendously improved the emission stability[186,187]. Lead halide perovskite QDs, by contrast, exhibit low spectral diffusion and blinking at cryogenic temperature[188], but at room temperature there is fluorescence intermittency[189], where shells are beneficial, too[190]. Furthermore, research on epitaxial QDs and 2D materials has created a manifold of techniques such as resonant excitation and encapsulation in crystalline matrices that could be adapted for colloidal QDs to further improve their performance[191,192].

Common metrics for characterizing single-photon sources are[193]: efficiency, measuring the fraction of the generated photons extracted into a usable mode; purity, expressing how multiphoton emission events disturb the single-photon emission; indistinguishability, quantifying the extent at which the created photons show genuine quantum interference on a beam splitter; and repetition rate, providing the rate at which individual photons can be generated. Associated with these metrics are distinct characterization methods and optimization routes[173]. The tell-tale signature of single-photon sources is photon antibunching[194,195], as can be observed in a Hanbury–Brown–Twiss set-up in which the light from the QD is split with a 50:50 beam splitter and then detected on two single-photon counters (Fig. 12a, top). As shown in Fig. 12a (bottom), the impurity is characterized by the deviation of the zero-time second-order autocorrelation $g^{(2)}(t = 0)$ from zero. QDs can achieve $g^{(2)}(t = 0) < 0.02$ (ref. 196) (Table 2), but the presence of multiple emissive states such as biexcitons[197], trions and fine-structure states[198] can increase impurity. Although near or far resonant optical excitation is the easiest and most often used method to drive QDs, electrical excitation – which has practical advantages for applications – is feasible[199]. A key property for many quantum optical applications is that indistinguishable photons are produced. Here, only very recently, it was possible to demonstrate this with lead halide colloidal QDs at cryogenic temperatures by observing Hong–Ou–Mandel interference on a beam splitter[198] (Fig. 12b).

Quantum dots in microcavities. An established way to improve the efficiency and purity of single-photon sources is the incorporation of QDs in optical microcavities[200], in which the Purcell effect fosters photon emission into the well-defined cavity mode. The Purcell effect occurs in the weak light–matter interaction regime where the loss rate from the cavity and spontaneous decay exceed the coupling rate between the light field and the excitons in the material. Single QDs have been embedded into microspheres[201], plasmonic nanocavities[202] and tunable, open microcavities[203], by which Purcell-enhanced emission with improved purity and emission rate was demonstrated.

In the strong light–matter interaction regime, the light–matter coupling rate dominates over the photonic and excitonic losses, and exciton polariton quasi-particles form whose wavefunction consists of part photon and part exciton. The energy spectrum acquires the characteristic anticrossing between the photonic and the excitonic state (Fig. 12c), and eventually at high excitation fluence, the polaritons spontaneously coalesce into a non-equilibrium Bose–Einstein condensate with macroscopical coherence[204]. As the exciton polaritons are a kind of interacting photons, the approach is attractive for quantum optical applications that require effective photon–photon interactions[205].

Exciton polaritons have been realized with colloidal II–VI QDs in tunable, open microcavities[206], even in solution[207] and more exotic realizations such as plasmonic hole arrays[208] as well as in structures that support bound-states-in-the-continuum[209]. Owing to their small inhomogeneous broadening and therefore lower excitonic disorder, colloidal II–VI nanoplatelets are an attractive material that has shown strong light–matter coupling and low-threshold room-temperature polariton condensation[210,211]. More recently, lead halide perovskite QDs have joined the family of polaritonic materials[212], in which polariton condensation has been observed in waveguides at cryogenic temperatures[213] and in a tunable, textured microcavity at room temperature[206,214].

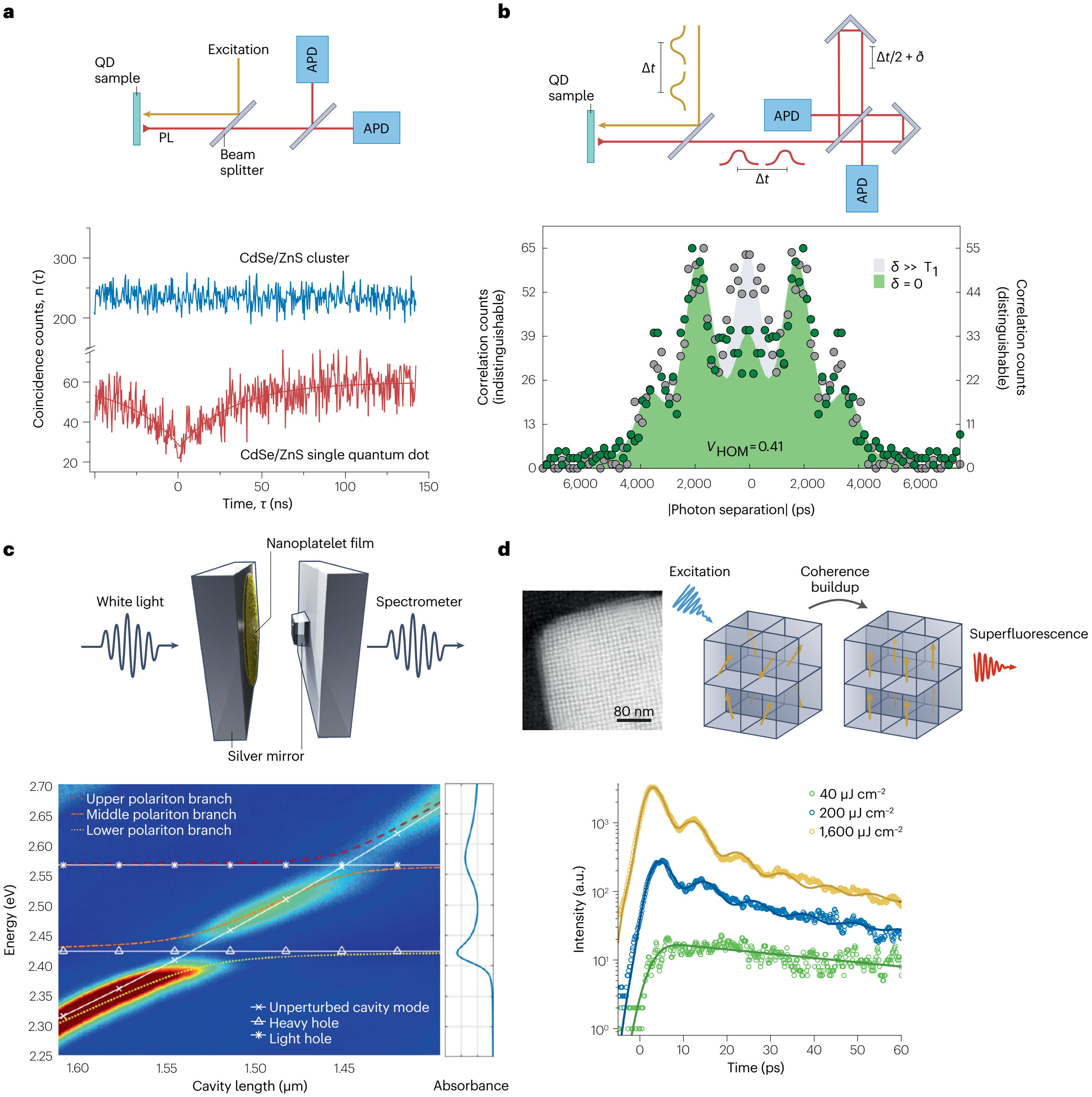

Coherence and collective quantum effects. A key property for quantum optical applications is the dephasing or decoherence of the electronic states[175]. The need for coherence is obvious in the context of qubits, in which a superposed or entangled quantum state should be preserved over a long time. However, decoherence also impacts single-photon emitters by reducing the indistinguishability of the generated photons and the coupling to microcavities by spectral broadening. Various physical effects lead to decoherence in colloidal QDs (Supplementary Information 10), of which some can be alleviated by using cryogenic cooling, whereas others are intrinsic to the material. Experimentally, four-wave mixing experiments allow to obtain the dephasing time T_2 on the ensemble level, yielding ~100 ps for II–VI (ref. 215) and tens of picoseconds for lead halide perovskite QDs at cryogenic temperatures[216] (Table 2). Furthermore, dephasing close to the fundamental limit of $T_2 = 2T_1$, with T_1 being the exciton decay time, was observed for some QDs[217,218].

Fig. 12 | Quantum optics with colloidal quantum dots. a, Using a Hanbury–Brown–Twiss set-up, the second-order correlation function of the emitted photon stream can be measured. Non-classical light emission from a single quantum emitter (here CdSe/ZnS quantum dots (QDs) at room temperature) exhibits characteristic antibunching with a deviation of the zero-time second-order autocorrelation $g^{(2)}(t = 0) < 0.5$, whereas an ensemble shows a flat correlation curve because thermal bunching occurs typically on timescales faster than the avalanche photodetector (APD) time resolution. **b**, Hong–Ou–Mandel (HOM) indistinguishability is measured by interfering subsequently generated photons with the same energy, polarization and spatial mode. With metal halide perovskite QDs at cryogenic temperature, the signal shows a dip at zero delay compared with distinguishable photons as both photons will coalesce on the beam splitter and propagate into the same APD. **c**, Integrating QDs in a tunable open microcavity enables the creation of exciton polaritons in the strong light–matter interaction regime as evidenced by the characteristic anticrossings between the excitonic and photonic states (here CdSe nanoplatelets at room temperature). **d**, Ordered QD superlattices can be formed through drying-mediated self-assembly. With metal halide perovskite QDs at sufficiently low temperature, the emitting dipoles can spontaneously synchronize their phases, giving rise to superfluorescent emission bursts, which can be observed by decay acceleration, superlinear peak intensity, delay shortening and Burnham–Chiao ringing. a.u., arbitrary unit; PL, photoluminescence; PNC, perovskite nanocrystal. Panel **a** adapted from ref. 290, Springer Nature Limited. Panel **b** adapted from ref. 198, Springer Nature Limited. Panel **c** adapted with permission from ref. 206, American Chemical Society. Panel **d** adapted from ref. 219, Springer Nature Limited.

With long-lasting coherence of the emitters, cooperative quantum effects such as superfluorescence can occur, where an ensemble of emitters spontaneously synchronizes the phase of their quantum state and collectively emits like an effective macroscopic emitter. Owing to the stringent requirements on homogeneous and inhomogeneous broadening as well as high oscillator strength, lead halide perovskite QDs stand out from both epitaxial and colloidal QDs. Supercrystal assemblies of $CsPbBr_3$ (ref. 219), also in the form of self-assembled whispering-gallery mode resonators[220], showed the key characteristics of superfluorescence (Fig. 12d): a delayed emission pulse with radiative decay acceleration and nonlinear peak intensity. Using binary superlattice assemblies allowed to control the lattice geometry and thereby the occurrence of superfluorescence[221]. These cooperative effects could be exploited to generate more complex multiphoton quantum states of light.

Reproducibility and data deposition

QDs are complex and sensitive materials, for which slight variations in synthesis, storage, measurement and processing conditions can have a significant impact on QD properties and device performance. Controlling the composition and structure of precursors and solvents used is an essential first step for reproducible QD research. Impure surfactants in a QD synthesis, such as tri-*n*-octylphosphine oxide, olelylamine and *n*-alkylphosphonic acids, can induce batch-to-batch variations in QD size, crystal structure or composition[222–224]. Although synthetically convenient, procedures that generate metal surfactant complexes in situ by liberating water have proven especially problematic. Despite extensive degassing, the Lewis acidity of these complexes retains water coproduct, which greatly influences the kinetics of precursor conversion[225]. Similarly, the combination of elemental chalcogens with octadecene and oleylamine produces complex mixtures that slowly change as volatile components are liberated, thereby influencing the precursor reactivity[226].

Eliminating sources of synthetic variability is essential to understanding precursor reactivity from a mechanistic perspective and making an informed choice about reagents and synthetic conditions. Abiding to such synthetic standards is also key to isolating QDs post synthesis with a well-defined surface termination. Contaminated surfactants can complicate the assignment of the surface structure, modify the ligand exchange reactivity[227] and cause beam damage during TEM imaging[228]. Moreover, work-up procedures can affect the ligand surface concentration or change the surface chemistry altogether, as shown for QD purification methods using alcohols as the non-solvent[229]. Given the importance of surface structure and ligand exchange reactions for QD processing, synthesis, purification and isolation methods can have a direct impact on device performance. Scientists in QD research should therefore heed reproducibility, by eliminating known sources of variability, drawing conclusions after duplicating experiments and duly reporting experimental procedures.

The heterogeneity of most QD ensembles leads to specific problems of misrepresentation when using methods that address QDs one-by-one. TEM, for example, provides unique information on single QDs, but deriving ensemble-averaged quantities from TEM images is far from straightforward. High-resolution studies should therefore always be complemented with lower magnification images to provide a reliable overview of the sample under investigation, and sample sizes for histograms analysis should be reported, containing at least 300 QDs[230,231]. Similar challenges arise in computational studies, in which relying on a single model structure can lead to biased conclusions. Multiple QD models, including possible conformers, should therefore be tested and compared by total energy, selecting the lowest-energy structure. This remains challenging for relatively large QDs, especially as ligands and solvent need to be included for the total energy calculations. Additionally, QD coordinates should be made publicly available in repositories such as GitHub or Zenodo, allowing testing and validation by computational scientists.

Finally, many of the metrics used to evaluate QD performance, as listed in Table 1, are derived from experimental studies with data that can be readily deposited, assessed for quality and reanalysed. This, however, is not the case for the PLQY, which is typically reported as a percentage without any reference to the underlying data or calibration procedures. Reliable PLQY measurements are much harder than is typically assumed, and large errors are easily made. Given the central role of this metric in QD research, PLQY certification, similar to the certification that is typical for solar cells[232], would be desirable, in particular for studies reporting near-unity values. The emerging photothermal threshold quantum yield method seems well suited for such a purpose[233].

Limitations and optimizations

Research on QDs has rapidly evolved from curiosity-inspired to technology-driven. Although synthetic methods proved scalable[234], the requirements imposed by various applications keep challenging QD research. This Primer highlights that QD-based devices can indeed be competitive in terms of performance but must be paired with operational stability and the use of non-restricted materials. Regulations, such as Europe's Restriction of Hazardous Substances directive, cap the amount of toxic elements, including Hg, Cd and Pb, electronic

Glossary

Auger recombination

Mechanism of non-radiative recombination of biexcitons, in which a first electron–hole pair recombines by transferring energy to a second electron–hole pair. The process becomes faster for electron–hole pairs confined in smaller volumes.

Band-edge transition

Electronic transition between the highest occupied molecular orbital (HOMO) and lowest unoccupied molecular orbital (LUMO) of a quantum dot. Terminology is derived from bulk semiconductor physics, in which the HOMO and LUMO are the states at the top of the valence and conduction bands, respectively.

Biexciton

Excited state of a quantum dot consisting of two electron–hole pairs.

Blinking

Emission characteristic of single quantum dots, involving sudden transitions between different levels of brightness.

Carrier cooling

Relaxation of a charge carrier to the band edges, the conduction band in the case of electrons and the valence band in the case of holes. Carrier cooling follows, for example, non-resonant photo-excitation.

Carrier trapping

Transfer of a charge carrier to a localized, lower-energy state.

Chromaticity diagram

A 2D representation that shows all the perceivable hues by the standard observer as (x, y) pairs, in which x and y measure the relative stimulation of standardized red and green light receptors, yielding the stimulation of the blue receptor as $1 - x - y$.

Colour rendering

Describes how an illuminant impacts the perceived colour, either consciously or subconsciously, by comparing the appearance of the colour with a standard illuminant. Quantified through the colour rendering index (CRI), in which a CRI of 90 is typically used as a benchmark for white light-emitting diodes.

Colour temperature

A parameter describing the colour of a visible light source by comparing it with the colour of light emitted by a black body radiator. Warm white light corresponds to colour temperature in the range 2,700–3,000 K.

Core/shell

Quantum dot geometry in which a core consisting of a first semiconductor is embedded within a shell of a second semiconductor.

Dephasing

Loss of quantum-mechanical coherence after optical excitation, resulting in the collapse of the state from a superposition into either the unexcited or the excited state. See also T_2 relaxation.

Detectivity

Figure of merit for a photodetector used to characterize performance, equal to the reciprocal of noise-equivalent power, normalized per square root of the area of the sensor and frequency bandwidth.

Diffusion

Transport of charge carriers caused by a gradient in the carrier concentration.

Drift

Transport of charge carriers caused by a force, typically an electric field.

Effective mass

Mass assigned to conduction-band electrons or valence-band holes to account for the impact of the crystal potential on the dynamics of motion.

Effective-mass approximation

A computational approach treating charge carriers as quasi particles characterized by an effective mass that accounts for the crystal potential. The effective-mass approximation, and the related $k\cdot p$ theory, describes quantized energy levels in quantum dots.

Energy transfer

Process by which an excited quantum system relaxes by the simultaneous excitation of a neighbouring quantum system. Energy transfer is induced by dipolar coupling and involves for two adjacent quantum dots the simultaneous recombination and formation of a band-edge exciton.

Exciton spin relaxation

Relaxation process that involves a change of spin or total angular momentum of the band-edge exciton. For example, cooling from the bright to the dark exciton state.

Excitons

The excited state of a quantum dot consisting of one electron–hole pair. The term is derived from solid-state physics, in which exciton describes a quasi-particle in a semiconductor that consists of an electron–hole pair bound through Coulomb interaction.

External quantum efficiency

(EQE). Figure of merit for a photodetector, defined as the ratio between the flux of photons incident on the photodiode and the resulting current of photogenerated charge carriers. An EQE of 100% means that for each absorbed photon, one charge carrier passes through the external circuit.

Luminescent colour conversion

Interpretation of photoluminescence as a method to convert the colour related to the higher energy absorbed by photons to the colour of the lower energy emitted by photons. Quantum dots have the advantage of converting light across a broad spectral range into a spectrally narrow emission, which corresponds to a saturated colour.

Luminescent solar concentrators

(LSCs). Device for concentrating sunlight for better solar energy conversion based on the re-emission by photoluminescence of absorbed sunlight under conditions of total internal reflection in a thin, transparent slab. Typically, solar cells are placed at the edges of the slab.

Monodisperse

Refers, in principle, to an ensemble of quantum dots with all the same size. In practice, a size dispersion below 5% is considered monodisperse.

Nanocolloids

Colloidal dispersion or suspension consisting of nanometre-sized solid particles in a liquid matrix.

Nuclear Overhauser effect

(nOe). Transfer of spin polarization between adjacent protons, in which the spin flip of a first proton is accompanied by the reverse spin flip of a neighbouring proton. The process is effective in molecules that tumble slowly in solution, such as ligands bound to quantum dots.

Nucleation

Part of the precipitation process that involves the formation of new nanocrystals out of the growth species or monomers. According to the classical nucleation theory, nucleation forms the smallest possible nanocrystals that are stable against redissolution.

Photoluminescence quantum yield

(PLQY). Ratio between the number of photons absorbed and emitted by a luminescent material. Typically expressed as a percentage and used as a measure of the internal efficiency of the photoluminescence, in which a PLQY of 100% implies that for each absorbed photon, one photon is re-emitted.

Glossary (continued)

Quantum confinement
A quantum mechanical effect by which the kinetic energy of a particle, such as an electron, increases when confined in a smaller volume.

Reorganization energy
Energy reduction related to the relaxation of a structure after charge transfer, for example, related to changes in local coordination.

Resonant excitation
Optical excitation of charge carriers across the bandgap where the photon energy matches the band-gap energy.

Responsivity
Figure of merit for a photodetector, defined as the ratio between the photocurrent and the incident optical power.

Sizing curves
A calibration curve that relates the energy gap of a quantum dot (QD) measured through absorption spectroscopy with the QD size. Transmission electron microscopy or small-angle X-ray scattering is typically used to determine the size of the QDs.

Spectral diffusion
Uninterrupted variation of the emission spectrum of single quantum dots, fluctuating back and forth around an average photon energy.

Spectral hole burning
The selective saturation of spin population with a narrow chemical shift range. In a heterogeneous resonance, this saturation creates a dent or spectral hole in the resonance.

Strong confinement
A regime of size quantization in which the quantization energy is the dominant contribution to the energy of electron–hole pairs.

Supersaturation
A state of a solution in which the solute concentration exceeds the solubility. Typically defined as the ratio between the solute concentration and the solubility.

Surface reconstructions
Reorganization of the atoms in a surface facet, forming a 2D lattice that is different from the corresponding bulk lattice plane.

T_2 relaxation
Loss of phase coherence between spins in the transversal plane.

Trap states
An electronic level within the energy gap separating the band of occupied and the band of unoccupied states. Such levels can provide a recombination pathway for an electron–hole pair, whereby these charge carriers are successively trapped in this state.

Wulff construction
A geometric method for predicting the equilibrium shape of a crystal by minimizing the total surface free energy. The distance between each surface facet and the crystal centre is taken proportional to the surface energy of the facet, so low-energy facets become dominant.

equipment can contain, and even when QD-based technologies can comply with maximum limits, concerns about public acceptance often translate into zero-Cd or zero-Pb policies. However, as indicated in the metrics listed in Tables 1 and 2, QDs based on CdSe, $CsPbBr_3$ or PbS generally perform better than non-restricted alternatives, such as InP and InAs-based QDs. For example, although InP/ZnSe/Zn QDs can attain near-unity PL efficiency in the visible, similar to CdSe and $CsPbBr_3$, their emission linewidth is relatively broad, biexciton lifetimes are short and exciton dephasing is fast. InAs QDs, active at wavelengths longer than 1,000 nm, exhibit a narrower spectral range, lower PL efficiency and reduced photodetection sensitivity than PbS QDs. Furthermore, although high-performance III–V/III–V core/shell QDs remain to be demonstrated, the III–V/II–VI hetero-interface is poorly understood[235], and operational stability of III–V QDs is not yet comparable to that of Cd-based and Pb-based QDs, hence the need for further research into new synthetic protocols for non-restricted QDs and the factors limiting performance and operational stability of QD devices.

Continued synthesis optimization could yield more monodisperse InP or InAs QDs, potentially addressing some of these differences. However, the current literature does not offer a general strategy to reduce size dispersion for a given synthesis. Other challenges appear to be more material-specific. For example, the concept of slowing down Auger recombination through graded interfaces has only been demonstrated in CdSe/CdS core/shell QDs, which therefore remain the most widely used for lasing applications. That said, the recent introduction of bulk-like nanocrystals, whose sizes are larger than the limit for strong quantization, may offer a possible alternative[236]. Furthermore, the formation of QD films with n-type or p-type character has been established for PbS QDs, but replicating these results with other QDs has proven difficult. One possible reason is that the facets of III–V semiconductors tend to form surface states[96,237]. Finally, the recent demonstration of indistinguishable photon emission appears to be specific to $CsPbBr_3$ nanocrystals, in which radiative recombination and exciton decoherence occur at similar rates under cryogenic conditions[198]. Reproducing this achievement with QDs emitting at other wavelengths remains an outstanding challenge.

Although performance is essential for QD technology, relatively few studies go beyond demonstrating performance to address stability under operational conditions of QDs and QD devices. Moreover, the few reported studies show that operational performance loss is a complex problem[238–240], involving issues intrinsic to QDs, to the interaction between QDs and ambient or the impact of QDs on other layers in a device stack. Moreover, results can be counterintuitive. Monitoring different LSCs in outdoor settings, for example, revealed a gradual degradation for CdSe-based LSCs but an improvement in performance for InP-based LSCs[240]. In many cases, the underlying failure processes remain poorly understood. As a result, synthesis optimizations aimed at improving stability lack a clear direction, which could limit the further development of QD technology.

Outlook

The field of colloidal QDs has shown a remarkable sequence of breakthrough results. Central to this development is the exceptional versatility of QDs as a material platform, in terms of materials addressed, tuning properties through structure and compatibility with analysis methods. Lead halide perovskites are only one example of many, where new semiconductors were readily formed as nanocolloids. Core/shell geometries, alloyed interfaces and surface termination are just three cases of structural adaptations that shifted the paradigm of QD technology. With little or no sample preparation, the same QDs can be analysed by techniques as diverse as solution NMR, STEM and femtosecond optical spectroscopy. Moreover, computational methods have been established that are increasingly capable of dealing with the complexity of QDs. We expect that the field will continue to use these unique capabilities to make headway and establish QDs as a competitive printable semiconductor in semiconductor and quantum technologies.

In the development of precisely controlled QDs, we foresee a major role for automated synthesis in combination with machine-learning (ML) approaches. QDs are a perfect model system for such approaches as synthesis and processing are possible in solution-based continuous flow or automated batch reactors[241–246]; critical properties and performance (particle size, particle size distribution and optical performance) can be easily and rapidly assessed via in situ optical spectroscopy, providing a reliable data set with direct feedback to the synthesis conditions, and reaction parameters can be controlled by tuning flow rates, concentrations and temperatures, providing a programmable feedback loop based on ML predictions of the measured parameters[245,247]. The combination of high-throughput screening and ML modelling can enable the discovery and optimization of QDs with unprecedented speed and accuracy. Such methods are expected to deliver rapid progress in the atomistic control of QD size, shape and surface composition. It will also allow screening of new core and shell materials as well as new surface ligands used in QDs.

The structure and properties of QDs are closely related, and the atomic precision of QD synthesis and analysis is therefore essential[248]. As showcased by the atomically precise thickness of colloidal nanoplatelets, atomic precision suppresses the heterogeneous broadening of properties such as the emission linewidth. Efforts to extend this atomic precision to different QD geometries, such as tetrahedrons, are ongoing[240]. This step is closely related to mechanistic understanding of QD growth during synthesis. A promising development is that the atomically precise analysis of the geometry of single QDs is increasingly realistic through real space imaging with STEM and diffractive imaging with pulsed coherent X-rays. Even in the absence of atomically precise ensembles, such methods will provide a new and detailed view on QD ensembles. Moreover, data on the atomistic structure of QDs will greatly help computational studies aimed at understanding structure–property relations.

Operational stability is a part of QD research in which more atomistic insight is needed. It is largely unknown how continuous loading — illumination, electric bias and ambient exposure — influences the QD properties by modifying the QD structure. Understanding and avoiding the underlying failure processes is essential for QD technology in the long run. For example, a recent study combining NMR with laser excitation showed that illumination induces desorption of oleate from CdSe QDs, a clear example of a failure process that offers insight in how to improve the stability[112]. A far more detailed picture on the relation among load, structural changes and failure can emerge if external stimuli are combined with in situ analysis methods that offer atomic precision, such as illumination in STEM[249]. Similarly, novel time-resolved electron and X-ray probes, derived from free electron lasers, X-ray synchrotron sources or pulsed electron accelerators, can provide insight into structural or chemical changes after optical or electrical pulses.

Ideally, such studies are supported by a computational framework that extends to QDs under load, and that can also capture rare processes that lead to failure. For this purpose, one can leverage ML force fields to perform long timescale molecular dynamics simulations. ML-based force fields, trained on accurate quantum mechanical data based on DFT, offer the ability to capture complex interatomic interactions with high accuracy while maintaining computational efficiency[250]. This capability is crucial for exploring the dynamics of QDs over extended periods, revealing how vacancy patterns, surface reconstructions and ligand arrangements evolve under various conditions. This approach can bridge the gap between current static DFT calculations and dynamic real-world conditions, while opening a path to complement real QDs by digital twins, whose development can be tracked as a function of time to map load, structural changes and failure relations. The result would be a more rational framework to direct QD synthesis, design QDs with tailored properties and enhance reproducibility and reliability in QD technology.

References

1. Rossetti, R., Nakahara, S. & Brus, L. E. Quantum size effects in the redox potentials, resonance Raman spectra, and electronic spectra of CdS crystallites in aqueous solution. *J. Chem. Phys.* **79**, 1086–1088 (1983).
   First report, to the best of our knowledge, on the observation of spectral blueshifts in dispersions of CdS nanocrystallites and their assignment to size quantization.
2. Ekimov, A. I. & Onushchenko, A. A. Quantum size effect in 3-dimensional microscopic semiconductor crystals. *JETP Lett.* **34**, 345–349 (1981).
3. Efros, A. L. & Brus, L. E. Nanocrystal quantum dots: from discovery to modern development. *ACS Nano* **15**, 6192–6210 (2021).
   Recent review of the development of the quantum dot research by two of the main scientists in the field.
4. Murray, C. B., Norris, D. J. & Bawendi, M. G. Synthesis and characterization of nearly monodisperse Cde (E = S, Se, Te) semiconductor nanocrystallites. *J. Am. Chem. Soc.* **115**, 8706–8715 (1993).
   First report, to the best of our knowledge, on the hot injection synthesis of monodisperse CdSe and CdS quantum dots. Starting point for colloidal quantum dot synthesis in organic solvents.
5. Efros, A. L. & Rosen, M. The electronic structure of semiconductor nanocrystals. *Annu. Rev. Mater. Sci.* **30**, 475–521 (2000).
6. Litvin, A. P. et al. Colloidal quantum dots for optoelectronics. *J. Mater. Chem. A* **5**, 13252–13275 (2017).
7. Carey, G. H. et al. Colloidal quantum dot solar cells. *Chem. Rev.* **115**, 12732–12763 (2015).
8. Karadza, B. et al. Bridging the green gap: monochromatic InP-based quantum-dot-on-chip LEDs with over 50% color conversion efficiency. *Nano Lett.* **23**, 5490–5496 (2023).
   Demonstration of monochromatic light-emitting diodes by on-chip colour conversion using InP-based quantum dots. Exemplifies opportunities and challenges of quantum dot colour conversion.
9. Won, Y.-H. et al. Highly efficient and stable InP/ZnSe/ZnS quantum dot light-emitting diodes. *Nature* **575**, 634–638 (2019).
   Demonstration of monochromatic light-emitting diodes by quantum dot electroluminescence using InP-based quantum dots.
10. Meinardi, F. et al. Large-area luminescent solar concentrators based on 'Stokes-shift-engineered' nanocrystals in a mass-polymerized PMMA matrix. *Nat. Photon.* **8**, 392–399 (2014).
11. Geiregat, P., Van Thourhout, D. & Hens, Z. A bright future for colloidal quantum dot lasers. *NPG Asia Mater.* **11**, 41 (2019).
12. Ahn, N. et al. Electrically driven amplified spontaneous emission from colloidal quantum dots. *Nature* **617**, 79–85 (2023).
   First demonstration, to the best of our knowledge, of an electrically driven quantum dot device showing stimulated emission.
13. García de Arquer, F. P. et al. Semiconductor quantum dots: technological progress and future challenges. *Science* **373**, eaaz8541 (2021).
14. Kim, J., Roh, J., Park, M. & Lee, C. Recent advances and challenges of colloidal quantum dot light-emitting diodes for display applications. *Adv. Mater.* **36**, 2212220 (2024).
15. Liu, J. et al. A near-infrared colloidal quantum dot imager with monolithically integrated readout circuitry. *Nat. Electron.* **5**, 443–451 (2022).
   Illustration of infrared imagers based on the integration of colloidal quantum dot photodiodes with silicon read-out electronics.
16. Shamsi, J., Urban, A. S., Imran, M., De Trizio, L. & Manna, L. Metal halide perovskite nanocrystals: synthesis, post-synthesis modifications, and their optical properties. *Chem. Rev.* **119**, 3296–3348 (2019).
17. Reiss, P., Carriere, M., Lincheneau, C., Vaure, L. & Tamang, S. Synthesis of semiconductor nanocrystals, focusing on nontoxic and earth-abundant materials. *Chem. Rev.* **116**, 10731–10819 (2016).
18. Sergeeva, K. A. et al. The rise of HgTe colloidal quantum dots for infrared optoelectronics. *Adv. Funct. Mater.* **34**, 2405307 (2024).
19. Hines, M. A. & Guyot-Sionnest, P. Synthesis and characterization of strongly luminescing ZnS-capped CdSe nanocrystals. *J. Phys. Chem.* **100**, 468–471 (1996).
   First report, to the best of our knowledge, on the synthesis of quantum dots with core/shell geometry and demonstration of the positive impact of shells on photoluminescence quantum yield. Starting point for all quantum dot applications involving light emission.
20. Kovalenko, M. V., Scheele, M. & Talapin, D. V. Colloidal nanocrystals with molecular metal chalcogenide surface ligands. *Science* **324**, 1417–1420 (2009).

21. Garcia-Santamaria, F. et al. Breakdown of volume scaling in Auger recombination in CdSe/CdS heteronanocrystals: the role of the core–shell interface. *Nano Lett.* **11**, 687–693 (2011).
Demonstration that Auger recombination can be suppressed in CdSe/CdS core/shell quantum dots, a result opening the way for quantum dot-based lasers and blinking-free emission by single quantum dots.
22. LaMer, V. K. & Dinegar, R. H. Theory, production and mechanism of formation of monodispersed hydrosols. *J. Am. Chem. Soc.* **72**, 4847–4854 (1950).
23. van Embden, J., Chesman, A. S. R. & Jasieniak, J. J. The heat-up synthesis of colloidal nanocrystals. *Chem. Mater.* **27**, 2246–2285 (2015).
24. Sugimoto, T., Shiba, F., Sekiguchi, T. & Itoh, H. Spontaneous nucleation of monodisperse silver halide particles from homogeneous gelatin solution I: silver chloride. *Colloid Surf. A* **164**, 183–203 (2000).
25. Owen, J. S., Chan, E. M., Liu, H. & Alivisatos, A. P. Precursor conversion kinetics and the nucleation of cadmium selenide nanocrystals. *J. Am. Chem. Soc.* **132**, 18206–18213 (2010).
26. Ruberu, T. P. A. et al. Molecular control of the nanoscale: effect of phosphine–chalcogenide reactivity on CdS–CdSe nanocrystal composition and morphology. *ACS Nano* **6**, 5348–5359 (2012).
27. Campos, M. P. et al. A library of selenourea precursors to PbSe nanocrystals with size distributions near the homogeneous limit. *J. Am. Chem. Soc.* **139**, 2296–2305 (2017).
28. Hendricks, M. P., Campos, M. P., Cleveland, G. T., Jen-La Plante, I. & Owen, J. S. A tunable library of substituted thiourea precursors to metal sulfide nanocrystals. *Science* **348**, 1226–1230 (2015).
Demonstration of size tuning at full yield in the hot injection synthesis by adjusting the reactivity of the precursors through chemical substitutions.
29. Guo, Y., Alvarado, S. R., Barclay, J. D. & Vela, J. Shape-programmed nanofabrication: understanding the reactivity of dichalcogenide precursors. *ACS Nano* **7**, 3616–3626 (2013).
30. McMurtry, B. M. et al. Continuous nucleation and size dependent growth kinetics of indium phosphide nanocrystals. *Chem. Mater.* **32**, 4358–4368 (2020).
31. Campos, M. P. et al. Growth kinetics determine the polydispersity and size of PbS and PbSe nanocrystals. *Chem. Sci.* **13**, 4555–4565 (2022).
32. Reiss, H. The growth of uniform colloidal dispersions. *J. Chem. Phys.* **19**, 482–487 (1951).
33. Peng, X. G., Wickham, J. & Alivisatos, A. P. Kinetics of II–VI and III–V colloidal semiconductor nanocrystal growth: 'focusing' of size distributions. *J. Am. Chem. Soc.* **120**, 5343–5344 (1998).
34. Bullen, C. R. & Mulvaney, P. Nucleation and growth kinetics of CdSe nanocrystals in octadecene. *Nano Lett.* **4**, 2303–2307 (2004).
35. Abécassis, B. et al. Persistent nucleation and size dependent attachment kinetics produce monodisperse PbS nanocrystals. *Chem. Sci.* **13**, 4977–4983 (2022).
36. Whitehead, C. B., Özkar, S. & Finke, R. G. LaMer's 1950 model for particle formation of instantaneous nucleation and diffusion-controlled growth: a historical look at the model's origins, assumptions, equations, and underlying sulfur sol formation kinetics data. *Chem. Mater.* **31**, 7116–7132 (2019).
37. Abécassis, B. et al. Real-time in situ probing of high-temperature quantum dots solution synthesis. *Nano Lett.* **15**, 2620–2626 (2015).
38. Prins, P. T. et al. Extended nucleation and superfocusing in colloidal semiconductor nanocrystal synthesis. *Nano Lett.* **21**, 2487–2496 (2021).
Description of the recent view on nucleation and growth in the hot injection synthesis, including the interplay between extended nucleation and size-dependent surface reactivity.
39. Mule, A. S. et al. Unraveling the growth mechanism of magic-sized semiconductor nanocrystals. *J. Am. Chem. Soc.* **143**, 2037–2048 (2021).
40. Weatherspoon, H. & Peters, B. Broken bond models, magic-sized clusters, and nucleation theory in nanoparticle synthesis. *J. Chem. Phys.* **158**, 114306 (2023).
41. Abécassis, B., Testard, F., Spalla, O. & Barboux, P. Probing in situ the nucleation and growth of gold nanoparticles by small-angle X-ray scattering. *Nano Lett.* **7**, 1723–1727 (2007).
42. Mozaffari, S. et al. The role of nanoparticle size and ligand coverage in size focusing of colloidal metal nanoparticles. *Nanoscale Adv.* **1**, 4052–4066 (2019).
43. Zhao, Q. & Kulik, H. J. Electronic structure origins of surface-dependent growth in III–V quantum dots. *Chem. Mater.* **30**, 7154–7165 (2018).
44. Prasad, B. L. V., Stoeva, S. I., Sorensen, C. M. & Klabunde, K. J. Digestive ripening of thiolated gold nanoparticles: the effect of alkyl chain length. *Langmuir* **18**, 7515–7520 (2002).
45. Shimpi, J. R., Sidhaye, D. S. & Prasad, B. L. V. Digestive ripening: a fine chemical machining process on the nanoscale. *Langmuir* **33**, 9491–9507 (2017).
46. Cassidy, J. et al. Enabling narrow emission line widths in colloidal nanocrystals through coalescence growth. *Chem. Mater.* **32**, 7524–7534 (2020).
47. Dong, Y. et al. Precise control of quantum confinement in cesium lead halide perovskite quantum dots via thermodynamic equilibrium. *Nano Lett.* **18**, 3716–3722 (2018).
48. Ithurria, S. et al. Colloidal nanoplatelets with two-dimensional electronic structure. *Nat. Mater.* **10**, 936–941 (2011).
49. Peng, X. G. et al. Shape control of CdSe nanocrystals. *Nature* **404**, 59–61 (2000).
50. Carbone, L. et al. Synthesis and micrometer-scale assembly of colloidal CdSe/CdS nanorods prepared by a seeded growth approach. *Nano Lett.* **7**, 2942–2950 (2007).
51. Tessier, M. D. et al. Efficient exciton concentrators built from colloidal core/crown CdSe/CdS semiconductor nanoplatelets. *Nano Lett.* **14**, 207–213 (2014).
52. Ekimov, A. I., Efros, A. L. & Onushchenko, A. A. Quantum size effect in semiconductor microcrystals. *Solid State Commun.* **56**, 921–924 (1985).
53. Brus, L. E. Electron–electron and electron–hole interactions in small semiconductor crystallites — the size dependence of the lowest excited electronic state. *J. Chem. Phys.* **80**, 4403–4409 (1984).
54. Brus, L. E. A simple-model for the ionization-potential, electron-affinity, and aqueous redox potentials of small semiconductor crystallites. *J. Chem. Phys.* **79**, 5566–5571 (1983).
55. Aubert, T. et al. General expression for the size-dependent optical properties of quantum dots. *Nano Lett.* **22**, 1778–1785 (2022).
56. Van Avermaet, H. et al. Full-spectrum InP-based quantum dots with near-unity photoluminescence quantum efficiency. *ACS Nano* **16**, 9701–9712 (2022).
57. Maes, J. et al. Size and concentration determination of colloidal nanocrystals by small-angle X-ray scattering. *Chem. Mater.* **30**, 3952–3962 (2018).
58. Rafipoor, M. et al. Strain engineering in InP/(Zn,Cd)Se core/shell quantum dots. *Chem. Mater.* **30**, 4393–4400 (2018).
59. Bals, S. et al. Three-dimensional atomic imaging of colloidal core–shell nanocrystals. *Nano Lett.* **11**, 3420–3424 (2011).
60. Midgley, P. A. & Weyland, M. 3D electron microscopy in the physical sciences: the development of Z-contrast and EFTEM tomography. *Ultramicroscopy* **96**, 413–431 (2003).
61. Han, Y. et al. Deep learning STEM-EDX tomography of nanocrystals. *Nat. Mach. Intell.* **3**, 267–274 (2021).
62. Albrecht, W., Van Aert, S. & Bals, S. Three-dimensional nanoparticle transformations captured by an electron microscope. *Acc. Chem. Res.* **54**, 1189–1199 (2021).
Overview of transmission electron microscopy methods for the 3D analysis of nanoparticles, including colloidal quantum dots.
63. Ophus, C. Four-dimensional scanning transmission electron microscopy (4D-STEM): from scanning nanodiffraction to ptychography and beyond. *Microsc. Microanal.* **25**, 563–582 (2019).
64. Clark, J. N., Huang, X., Harder, R. & Robinson, I. K. High-resolution three-dimensional partially coherent diffraction imaging. *Nat. Commun.* **3**, 993 (2012).
65. Estandarte, A. K. C. et al. Bragg coherent diffraction imaging of iron diffusion into gold nanocrystals. *N. J. Phys.* **20**, 113026 (2018).
66. Liu, H. et al. Visualization of plasmonic couplings using ultrafast electron microscopy. *Nano Lett.* **21**, 5842–5849 (2021).
67. Alcorn, F. M., Jain, P. K. & van der Veen, R. M. Time-resolved transmission electron microscopy for nanoscale chemical dynamics. *Nat. Rev. Chem.* **7**, 256–272 (2023).
68. van der Veen, R. M., Kwon, O.-H., Tissot, A., Hauser, A. & Zewail, A. H. Single-nanoparticle phase transitions visualized by four-dimensional electron microscopy. *Nat. Chem.* **5**, 395–402 (2013).
69. Moonsub, S. & Philippe, G.-S. Permanent dipole moment and charges in colloidal semiconductor quantum dots. *J. Chem. Phys.* **111**, 6955–6964 (1999).
70. Cirillo, M., Strubbe, F., Neyts, K. & Hens, Z. Thermal charging of colloidal quantum dots in apolar solvents: a current transient analysis. *ACS Nano* **5**, 1345–1352 (2011).
71. Taylor, J., Kippeny, T. & Rosenthal, S. J. Surface stoichiometry of CdSe nanocrystals determined by Rutherford backscattering spectroscopy. *J. Clust. Sci.* **12**, 571–582 (2001).
72. Capek, R. K. et al. Optical properties of zincblende cadmium selenide quantum dots. *J. Phys. Chem. C* **114**, 6371–6376 (2010).
73. Fritzinger, B., Capek, R. K., Lambert, K., Martins, J. C. & Hens, Z. Utilizing self-exchange to address the binding of carboxylic acid ligands to CdSe quantum dots. *J. Am. Chem. Soc.* **132**, 10195–10201 (2010).
74. Anderson, N. C. & Owen, J. S. Soluble, chloride-terminated CdSe nanocrystals: ligand exchange monitored by H-1 and P-31 NMR spectroscopy. *Chem. Mater.* **25**, 69–76 (2013).
75. Hens, Z. Ligands on nanocrystal surfaces, the H-1 nuclear magnetic resonance fingerprint. *Acc. Chem. Res.* **56**, 1623–1633 (2023).
Review of solution NMR spectroscopy methods for the analysis of quantum dot surfaces.
76. Hens, Z., Moreels, I. & Martins, J. C. In situ H-1 NMR study on the trioctylphosphine oxide capping of colloidal InP nanocrystals. *ChemPhysChem* **6**, 2578–2584 (2005).
77. De Roo, J. et al. Probing solvent–ligand interactions in colloidal nanocrystals by the NMR line broadening. *Chem. Mater.* **30**, 5485–5492 (2018).
78. Fritzinger, B. et al. In situ observation of rapid ligand exchange in colloidal nanocrystal suspensions using transfer NOE nuclear magnetic resonance spectroscopy. *J. Am. Chem. Soc.* **131**, 3024 (2009).
79. Cros-Gagneux, A. et al. Surface chemistry of InP quantum dots: a comprehensive study. *J. Am. Chem. Soc.* **132**, 18147–18157 (2010).
80. Piveteau, L. et al. Structure of colloidal quantum dots from dynamic nuclear polarization surface enhanced NMR spectroscopy. *J. Am. Chem. Soc.* **137**, 13964–13971 (2015).
81. De Nolf, K. et al. Binding and packing in two-component colloidal quantum dot ligand shells: linear versus branched carboxylates. *J. Am. Chem. Soc.* **139**, 3456–3464 (2017).
82. Anderson, N. C., Hendricks, M. P., Choi, J. J. & Owen, J. S. Ligand exchange and the stoichiometry of metal chalcogenide nanocrystals: spectroscopic observation of facile metal-carboxylate displacement and binding. *J. Am. Chem. Soc.* **135**, 18536–18548 (2013).
83. Drijvers, E., De Roo, J., Martins, J. C., Infante, I. & Hens, Z. Ligand displacement exposes binding site heterogeneity on CdSe nanocrystal surfaces. *Chem. Mater.* **30**, 1178–1186 (2018).

84. Singh, S., Leemans, J., Zaccaria, F., Infante, I. & Hens, Z. Ligand adsorption energy and the postpurification surface chemistry of colloidal metal chalcogenide nanocrystals. *Chem. Mater.* **33**, 2796–2803 (2021).
85. Efros, A. L. et al. Band-edge exciton in quantum dots of semiconductors with a degenerate valence band: dark and bright exciton states. *Phys. Rev. B* **54**, 4843–4856 (1996).
86. Zunger, A. Electronic-structure theory of semiconductor quantum dots. *MRS Bull.* **23**, 35–42 (1998).
87. Niquet, Y. M., Delerue, C., Allan, G. & Lannoo, M. Method for tight-binding parametrization: application to silicon nanostructures. *Phys. Rev. B* **62**, 5109–5116 (2000).
88. Chatzigoulas, A., Karathanou, K., Dellis, D. & Cournia, Z. NanoCrystal: a web-based crystallographic tool for the construction of nanoparticles based on their crystal habit. *J. Chem. Inform. Model.* **58**, 2380–2386 (2018).
89. Voznyy, O. Mobile surface traps in CdSe nanocrystals with carboxylic acid ligands. *J. Phys. Chem. C* **115**, 15927–15932 (2011).
90. Houtepen, A. J., Hens, Z., Owen, J. S. & Infante, I. On the origin of surface traps in colloidal II–VI semiconductor nanocrystals. *Chem. Mater.* **29**, 752–761 (2017).
First demonstration, to the best of our knowledge, by density functional theory of the relation between a geometrical feature and electronic trap states. Inspired multiple approaches for post-synthesis enhancement of the photoluminescence quantum yield.
91. Dümbgen, K. C., Zito, J., Infante, I. & Hens, Z. Shape, electronic structure, and trap states in indium phosphide quantum dots. *Chem. Mater.* **33**, 6885–6896 (2021).
92. Leemans, J. et al. Near-edge ligand stripping and robust radiative exciton recombination in CdSe/CdS core/crown nanoplatelets. *J. Phys. Chem. Lett.* **11**, 3339–3344 (2020).
93. Kirkwood, N. et al. Finding and fixing traps in II–VI and III–V colloidal quantum dots: the importance of Z-type ligand passivation. *J. Am. Chem. Soc.* **140**, 15712–15723 (2018).
94. Llusar, J., du Fossé, I., Hens, Z., Houtepen, A. & Infante, I. Surface reconstructions in II–VI quantum dots. *ACS Nano* **18**, 1563–1572 (2024).
95. Lannoo, M. Basic principles governing the surface atomic-structure of zinc blende semiconductors. *Mat. Sci. Eng. B* **22**, 1–8 (1993).
96. Hens, Z., Llusar, J. & Infante, I. Fuzzy band structure of quantum dots by Bloch orbital expansion: unconventional insights into geometric–electronic structure relations. *ACS Nano* **19**, 8227–8237 (2025).
97. Geiregat, P. et al. The impact of partial carrier confinement on stimulated emission in strongly confined perovskite nanocrystals. *ACS Nano* **18**, 17794–17805 (2024).
98. Klimov, V. I. Optical nonlinearities and ultrafast carrier dynamics in semiconductor nanocrystals. *J. Phys. Chem. B* **104**, 6112–6123 (2000).
99. Rogach, A. L., Klar, T. A., Lupton, J. M., Meijerink, A. & Feldmann, J. Energy transfer with semiconductor nanocrystals. *J. Mater. Chem.* **19**, 1208–1221 (2009).
100. Bender, J. A. et al. Surface states mediate triplet energy transfer in nanocrystal–acene composite systems. *J. Am. Chem. Soc.* **140**, 7543–7553 (2018).
101. Li, Q. et al. Charge transfer from quantum-confined 0D, 1D, and 2D nanocrystals. *Chem. Rev.* **124**, 5695–5763 (2024).
102. Klimov, V. I. Spectral and dynamical properties of multiexcitons in semiconductor nanocrystals. *Annu. Rev. Phys. Chem.* **58**, 635 (2007).
Overview of ultrafast optical spectroscopy methods for the analysis of the photo-excited states of colloidal quantum dots, with an emphasis on multi-exciton properties.
103. Geiregat, P. et al. Thermodynamic equilibrium between excitons and excitonic molecules dictates optical gain in colloidal CdSe quantum wells. *J. Phys. Chem. Lett.* **10**, 3637–3644 (2019).
104. Beavon, J. et al. Quantum shells versus quantum dots: suppressing Auger recombination in colloidal semiconductors. *Chem. Comm.* **59**, 11337–11348 (2023).
105. Yang, W., Liu, Y., McBride, J. R. & Lian, T. Ultrafast and long-lived transient heating of surface adsorbates on plasmonic semiconductor nanocrystals. *Nano Lett.* **21**, 453–461 (2021).
106. Kennehan, E. R. et al. Dynamic ligand surface chemistry of excited PbS quantum dots. *J. Phys. Chem. Lett.* **11**, 2291–2297 (2020).
107. Diroll, B. T., Guo, P. & Schaller, R. D. Heat transfer at hybrid interfaces: interfacial ligand-to-nanocrystal heating monitored with infrared pump, electronic probe spectroscopy. *Nano Lett.* **18**, 7863–7869 (2018).
108. Beecher, A. N. et al. Atomic structures and gram scale synthesis of three tetrahedral quantum dots. *J. Am. Chem. Soc.* **136**, 10645–10653 (2014).
109. Gary, D. C. et al. Single-crystal and electronic structure of a 1.3 nm indium phosphide nanocluster. *J. Am. Chem. Soc.* **138**, 1510–1513 (2016).
110. Goldstein, A. N., Echer, C. M. & Alivisatos, A. P. Melting in semiconductor nanocrystals. *Science* **256**, 1425–1427 (1992).
111. Smith, A. M., Mohs, A. M. & Nie, S. Tuning the optical and electronic properties of colloidal nanocrystals by lattice strain. *Nat. Nanotechnol.* **4**, 56–63 (2009).
112. Harvey, S. M. et al. Ligand desorption and fragmentation in oleate-capped CdSe nanocrystals under high-intensity photoexcitation. *J. Am. Chem. Soc.* **146**, 3732–3741 (2024).
113. Plech, A. et al. Physical regimes and mechanisms of picosecond laser fragmentation of gold nanoparticles in water from X-ray probing and atomistic simulations. *ACS Nano* **18**, 10527–10541 (2024).
114. Seiler, H. et al. Direct observation of ultrafast lattice distortions during exciton-polaron formation in lead halide perovskite nanocrystals. *ACS Nano* **17**, 1979–1988 (2023).
115. Kirschner, M. S. et al. Transient melting and recrystallization of semiconductor nanocrystals under multiple electron–hole pair excitation. *Nano Lett.* **17**, 5314–5320 (2017).
116. Szilagyi, E. et al. Visualization of nanocrystal breathing modes at extreme strains. *Nat. Commun.* **6**, 6577 (2015).
117. Leonard, A. A. et al. Light-Induced transient lattice dynamics and metastable phase transition in CH3NH3PbI3 nanocrystals. *ACS Nano* **17**, 5306–5315 (2023).
118. Ruan, C.-Y. et al. The development and applications of ultrafast electron nanocrystallography. *Microsc. Microanal.* **15**, 323–337 (2009).
119. Miller, R. J. D. Femtosecond crystallography with ultrabright electrons and X-rays: capturing chemistry in action. *Science* **343**, 1108–1116 (2014).
120. Guzelturk, B. et al. Dynamic lattice distortions driven by surface trapping in semiconductor nanocrystals. *Nat. Commun.* **12**, 1860 (2021).
121. Kirschner, M. S. et al. Photoinduced, reversible phase transitions in all-inorganic perovskite nanocrystals. *Nat. Commun.* **10**, 504 (2019).
122. Nirmal, M. et al. Observation of the dark exciton in CdSe quantum dots. *Phys. Rev. Lett.* **75**, 3728–3731 (1995).
123. Shornikova, E. V. et al. Addressing the exciton fine structure in colloidal nanocrystals: the case of CdSe nanoplatelets. *Nanoscale* **10**, 646–656 (2018).
124. Brodu, A. et al. Fine structure of nearly isotropic bright excitons in InP/ZnSe colloidal quantum dots. *J. Phys. Chem. Lett.* **10**, 5468–5475 (2019).
125. Crooker, S. A., Barrick, T., Hollingsworth, J. A. & Klimov, V. I. Multiple temperature regimes of radiative decay in CdSe nanocrystal quantum dots: intrinsic limits to the dark-exciton lifetime. *Appl. Phys. Lett.* **82**, 2793–2795 (2003).
126. Biadala, L. et al. Band-edge exciton fine structure and recombination dynamics in InP/ZnS colloidal nanocrystals. *ACS Nano* **10**, 3356–3364 (2016).
127. Moreels, I. et al. Band-edge exciton fine structure of small, nearly spherical colloidal CdSe/ZnS quantum dots. *ACS Nano* **5**, 8033–8039 (2011).
128. Nirmal, M. et al. Fluorescence intermittency in single cadmium selenide nanocrystals. *Nature* **383**, 802–804 (1996).
129. Empedocles, S. A., Norris, D. J. & Bawendi, M. G. Photoluminescence spectroscopy of single CdSe nanocrystallite quantum dots. *Phys. Rev. Lett.* **77**, 3873–3876 (1996).
130. Marzin, J. Y., Gérard, J. M., Izraël, A., Barrier, D. & Bastard, G. Photoluminescence of single InAs quantum dots obtained by self-organized growth on GaAs. *Phys. Rev. Lett.* **73**, 716–719 (1994).
131. Tamarat, P., Maali, A., Lounis, B. & Orrit, M. Ten years of single-molecule spectroscopy. *J. Phys. Chem. A* **104**, 1–16 (2000).
132. Htoon, H., Cox, P. J. & Klimov, V. I. Structure of excited-state transitions of individual semiconductor nanocrystals probed by photoluminescence excitation spectroscopy. *Phys. Rev. Lett.* **93**, 187402 (2004).
133. Cui, J. et al. Direct probe of spectral inhomogeneity reveals synthetic tunability of single-nanocrystal spectral linewidths. *Nat. Chem.* **5**, 602 (2013).
134. Malinowski, P. E. et al. Thin-film quantum dot photodiode for monolithic infrared image. *Sens. Sensors* **17**, 10 (2017).
135. Vafaie, M. et al. Colloidal quantum dot photodetectors with 10-ns response time and 80% quantum efficiency at 1,550 nm. *Matter* **4**, 1042–1053 (2021).
Illustration of state-of-the-art quantum dot photodetectors active in the short-wave infrared.
136. Bard, A. J. & Faulkner, L. R. *Electrochemical Methods: Fundamentals and Applications*, 2nd edn (Wiley, 2000).
137. Sandeep, C. S. S. et al. Epitaxially connected PbSe quantum-dot films: controlled neck formation and optoelectronic properties. *ACS Nano* **8**, 11499–11511 (2014).
138. Talgorn, E. et al. Unity quantum yield of photogenerated charges and band-like transport in quantum-dot solids. *Nat. Nanotechnol.* **6**, 733–739 (2011).
139. Lee, J.-S., Kovalenko, M. V., Huang, J., Chung, D. S. & Talapin, D. V. Band-like transport, high electron mobility and high photoconductivity in all-inorganic nanocrystal arrays. *Nat. Nanotechnol.* **6**, 348–352 (2011).
Demonstration of high mobility charge-carrier transport in quantum dot films, achieved by replacing as-synthesized long organic ligands by short inorganic moieties.
140. Choi, J.-H. et al. Bandlike transport in strongly coupled and doped quantum dot solids: a route to high-performance thin-film electronics. *Nano Lett.* **12**, 2631–2638 (2012).
141. Roest, A. L., Kelly, J. J., Vanmaekelbergh, D. & Meulenkamp, E. A. Staircase in the electron mobility of a ZnO quantum dot assembly due to shell filling. *Phys. Rev. Lett.* **89**, 036801 (2002).
142. Yu, D., Wang, C. J. & Guyot-Sionnest, P. n-type conducting CdSe nanocrystal solids. *Science* **300**, 1277–1280 (2003).
143. Talapin, D. V. & Murray, C. B. PbSe nanocrystal solids for n- and p-channel thin film field-effect transistors. *Science* **310**, 86–89 (2005).
144. Nugraha, M. I. et al. Recent progress in colloidal quantum dot thermoelectrics. *Adv. Mater.* **35**, 2210683 (2023).
145. Baek, G. W. et al. Memristive switching mechanism in colloidal InP/ZnSe/ZnS quantum dot-based synaptic devices for neuromorphic computing. *Nano Lett.* **24**, 5855–5861 (2024).
146. Khan, J., Ullah, I. & Yuan, J. $CsPbI_3$ perovskite quantum dot solar cells: opportunities, progress and challenges. *Mater. Adv.* **3**, 1931–1952 (2022).
147. Huang, H. et al. High-efficiency perovskite quantum dot photovoltaic with homogeneous structure and energy landscape. *Adv. Funct. Mater.* **33**, 2210728 (2023).
148. Liu, M. et al. Colloidal quantum dot electronics. *Nat. Electron.* **4**, 548–558 (2021).
Overview of quantum dot applications, including optical down conversion and optoelectronic devices.

149. Guo, R. et al. Advances in colloidal quantum dot-based photodetectors. *J. Mater. Chem. C* **10**, 7404–7422 (2022).
150. Osypiw, A. R. C. et al. Solution-processed colloidal quantum dots for light emission. *Mater. Adv.* **3**, 6773–6790 (2022).
151. Proppe, A. H. et al. Highly stable and pure single-photon emission with 250 ps optical coherence times in InP colloidal quantum dots. *Nat. Nanotechnol.* **18**, 993–999 (2023).
152. Chen, J., Zhao, Q., Yu, B. & Lemmer, U. A review on quantum dot-based color conversion layers for mini/micro-LED displays: packaging, light management, and pixelation. *Adv. Opt. Mater.* **12**, 2300873 (2024).
153. Sliz, R. et al. Stable colloidal quantum dot inks enable inkjet-printed high-sensitivity infrared photodetectors. *ACS Nano* **13**, 11988–11995 (2019).
154. Jang, E. et al. White-light-emitting diodes with quantum dot color converters for display backlights. *Adv. Mater.* **22**, 3076–3080 (2010).
155. Zhu, R. D., Luo, Z. Y., Chen, H. W., Dong, Y. J. & Wu, S. T. Realizing Rec. 2020 color gamut with quantum dot displays. *Opt. Express* **23**, 23680–23693 (2015).
156. Erdem, T. & Demir, H. V. Color science of nanocrystal quantum dots for lighting and displays. *Nanophotonics* **2**, 57–81 (2013).
157. Liu, Z. et al. Micro-light-emitting diodes with quantum dots in display technology. *Light-Sci. Appl.* **9**, 83 (2020).
Review of the opportunities of using colloidal quantum dots as the colour convertor in micro-light-emitting diode displays.
158. Steckel, J. S. et al. Quantum dots: the ultimate down-conversion material for LCD displays. *J. Soc. Inform. Disp.* **23**, 294–305 (2015).
159. Shimizu, K. T. et al. Toward commercial realization of quantum dot based white light-emitting diodes for general illumination. *Photon. Res.* **5**, A1–A6 (2017).
160. Karadza, B., Van Avermaet, H., Mingabudinova, L., Hens, Z. & Meuret, Y. Efficient, high-CRI white LEDs by combining traditional phosphors with cadmium-free InP/ZnSe red quantum dots. *Photon. Res.* **10**, 155–165 (2022).
161. Deng, Y.-H. et al. Short-wave infrared colloidal QD photodetector with nanosecond response times enabled by ultrathin absorber layers. *Adv. Mater.* **36**, 2402002 (2024).
162. Shilpa, G. et al. Recent advances in the development of high efficiency quantum dot sensitized solar cells (QDSSCs): a review. *Mater. Sci. Energy Technol.* **6**, 533–546 (2023).
163. Carvalho Junior, J. A., Nunes, C. L., Machado, W. S. & Schiavon, M. A. Recent progresses in quantum-dot-sensitized solar cells: the role of counter electrodes. *Energy Technol.* **12**, 2400254 (2024).
164. Hu, L. & Mandelis, A. Advanced characterization methods of carrier transport in quantum dot photovoltaic solar cells. *J. Appl. Phys.* **129**, 091101 (2021).
165. Zhang, Z. et al. Dual ligand capped quantum dots improving loading amount for high-efficiency quantum dot-sensitized solar cells. *ACS Energy Lett.* **8**, 647–656 (2023).
166. Zhang, Z., Wang, W., Rao, H., Pan, Z. & Zhong, X. Boosting the efficiency of quantum dot-sensitized solar cells over 17% via sequential deposition of water- and oil-soluble quantum dots. *Adv. Funct. Mater.* https://doi.org/10.1002/adfm.202501241 (2025).
167. Du, Z. & Ma, D. Recent progress in I–III–VI colloidal quantum dots-integrated solar cells. *Curr. Opin. Colloid Interface Sci.* **75**, 101890 (2025).
168. Jang, E. & Jang, H. Review: quantum dot light-emitting diodes. *Chem. Rev.* **123**, 4663–4692 (2023).
Review of electroluminescent quantum dot light-emitting diode technology.
169. Chen, Z. et al. Color revolution: prospects and challenges of quantum-dot light-emitting diode display technologies. *Small Methods* **8**, 2300359 (2024).
170. Deng, Y. et al. Solution-processed green and blue quantum-dot light-emitting diodes with eliminated charge leakage. *Nat. Photon.* **16**, 505–511 (2022).
171. Song, J. et al. Over 30% external quantum efficiency light-emitting diodes by engineering quantum dot-assisted energy level match for hole transport layer. *Adv. Funct. Mater.* **29**, 1808377 (2019).
172. Haroche, S. & Raimond, J.-M. *Exploring the Quantum: Atoms, Cavities, and Photons* (Oxford Univ. Press, 2006).
173. Senellart, P., Solomon, G. & White, A. High-performance semiconductor quantum-dot single-photon sources. *Nat. Nanotechnol.* **12**, 1026–1039 (2017).
174. Kagan, C. R., Bassett, L. C., Murray, C. B. & Thompson, S. M. Colloidal quantum dots as platforms for quantum information science. *Chem. Rev.* **121**, 3186–3233 (2021).
175. Zhu, J., Li, Y., Lin, X., Han, Y. & Wu, K. Coherent phenomena and dynamics of lead halide perovskite nanocrystals for quantum information technologies. *Nat. Mater.* **23**, 1027–1040 (2024).
176. Couteau, C. et al. Applications of single photons to quantum communication and computing. *Nat. Rev. Phys.* **5**, 326–338 (2023).
177. Maring, N. et al. A versatile single-photon-based quantum computing platform. *Nat. Photon.* **18**, 603–609 (2024).
178. Tomm, N. et al. A bright and fast source of coherent single photons. *Nat. Nanotechnol.* **16**, 399–403 (2021).
179. Reinhard, A. et al. Strongly correlated photons on a chip. *Nat. Photon.* **6**, 93–96 (2012).
180. Blanton, S. A., Hines, M. A. & Guyot-Sionnest, P. Photoluminescence wandering in single CdSe nanocrystals. *Appl. Phys. Lett.* **69**, 3905–3907 (1996).
181. Efros, A. L. & Rosen, M. Random telegraph signal in the photoluminescence intensity of a single quantum dot. *Phys. Rev. Lett.* **78**, 1110–1113 (1997).
182. Neuhauser, R. G., Shimizu, K. T., Woo, W. K., Empedocles, S. A. & Bawendi, M. G. Correlation between fluorescence intermittency and spectral diffusion in single semiconductor quantum dots. *Phys. Rev. Lett.* **85**, 3301–3304 (2000).
183. Fernée, M. J. et al. Spontaneous spectral diffusion in CdSe quantum dots. *J. Phys. Chem. Lett.* **3**, 1716–1720 (2012).
184. Utzat, H. & Bawendi, M. G. Lifetime-resolved photon-correlation Fourier spectroscopy. *Opt. Express* **29**, 14293–14303 (2021).
185. Brokmann, X., Marshall, L. & Bawendi, M. Revealing single emitter spectral dynamics from intensity correlations in an ensemble fluorescence spectrum. *Opt. Express* **17**, 4509–4517 (2009).
186. Mahler, B. et al. Towards non-blinking colloidal quantum dots. *Nat. Mater.* **7**, 659–664 (2008).
187. Cheng, Y. et al. Continuously graded quantum dots: synthesis, applications in quantum dot light-emitting diodes, and perspectives. *J. Phys. Chem. Lett.* **12**, 5967–5978 (2021).
188. Raino, G. et al. Single cesium lead halide perovskite nanocrystals at low temperature: fast single photon emission, reduced blinking, and exciton fine structure. *ACS Nano* **10**, 2485–2490 (2016).
189. Park, Y. S., Guo, S. J., Makarov, N. S. & Klimov, V. I. Room temperature single-photon emission from individual perovskite quantum dots. *ACS Nano* **9**, 10386–10393 (2015).
190. Rainò, G. et al. Ultra-narrow room-temperature emission from single CsPbBr$_3$ perovskite quantum dots. *Nat. Commun.* **13**, 2587 (2022).
191. Heindel, T., Kim, J.-H., Gregersen, N., Rastelli, A. & Reitzenstein, S. Quantum dots for photonic quantum information technology. *Adv. Opt. Photon.* **15**, 613–738 (2023).
192. Turunen, M. et al. Quantum photonics with layered 2D materials. *Nat. Rev. Phys.* **4**, 219–236 (2022).
193. Aharonovich, I., Englund, D. & Toth, M. Solid-state single-photon emitters. *Nat. Photon.* **10**, 631–641 (2016).
194. Lounis, B., Bechtel, H. A., Gerion, D., Alivisatos, P. & Moerner, W. E. Photon antibunching in single CdSe/ZnS quantum dot fluorescence. *Chem. Phys. Lett.* **329**, 399–404 (2000).
195. Messin, G., Hermier, J. P., Giacobino, E., Desbiolles, P. & Dahan, M. Bunching and antibunching in the fluorescence of semiconductor nanocrystals. *Opt. Lett.* **26**, 1891–1893 (2001).
196. Zhu, C. et al. Room-temperature, highly pure single-photon sources from all-inorganic lead halide perovskite quantum dots. *Nano Lett.* **22**, 3751–3760 (2022).
197. Nair, G., Zhao, J. & Bawendi, M. G. Biexciton quantum yield of single semiconductor nanocrystals from photon statistics. *Nano Lett.* **11**, 1136–1140 (2011).
198. Kaplan, A. E. K. et al. Hong–Ou–Mandel interference in colloidal CsPbBr$_3$ perovskite nanocrystals. *Nat. Photon.* **17**, 775–780 (2023).
Demonstraton of sequential emission of indisinguishable photons by single CsPbBr$_3$ nanocrystals, a milestone for the application of quantum dots in quantum optics.
199. Lin, X. et al. Electrically-driven single-photon sources based on colloidal quantum dots with near-optimal antibunching at room temperature. *Nat. Commun.* **8**, 1132 (2017).
200. Gérard, J. M. et al. Enhanced spontaneous emission by quantum boxes in a monolithic optical microcavity. *Phys. Rev. Lett.* **81**, 1110–1113 (1998).
201. Le Thomas, N. et al. Cavity QED with semiconductor nanocrystals. *Nano Lett.* **6**, 557–561 (2006).
202. Hoang, T. B., Akselrod, G. M. & Mikkelsen, M. H. Ultrafast room-temperature single photon emission from quantum dots coupled to plasmonic nanocavities. *Nano Lett.* **16**, 270–275 (2016).
203. Farrow, T. et al. Ultranarrow line width room-temperature single-photon source from perovskite quantum dot embedded in optical microcavity. *Nano Lett.* **23**, 10667–10673 (2023).
204. Carusotto, I. & Ciuti, C. Quantum fluids of light. *Rev. Mod. Phys.* **85**, 299–366 (2013).
205. Moxley, F. I., Ilo-Okeke, E. O., Mudaliar, S. & Byrnes, T. Quantum technology applications of exciton–polariton condensates. *Emergent Mater.* **4**, 971–988 (2021).
206. Flatten, L. C. et al. Strong exciton–photon coupling with colloidal nanoplatelets in an open microcavity. *Nano Lett.* **16**, 7137–7141 (2016).
207. Dovzhenko, D. et al. Strong exciton–photon coupling with colloidal quantum dots in a tunable microcavity. *Appl. Phys. Lett.* **119**, 011102 (2021).
208. Winkler, J. M. et al. Room-temperature strong coupling of CdSe nanoplatelets and plasmonic hole arrays. *Nano Lett.* **19**, 108–115 (2019).
209. Zhen, Z., Jin, S.-Y., Jie, R., Liang, H.-Y. & Xu, X.-S. Strong coupling between colloidal quantum dots and a microcavity with hybrid structure at room temperature. *Photon. Res.* **10**, 913–921 (2022).
210. Qiu, L. et al. Molecular polaritons generated from strong coupling between CdSe nanoplatelets and a dielectric optical cavity. *J. Phys. Chem. Lett.* **12**, 5030–5038 (2021).
211. Yang, H. et al. Ultralow threshold room temperature polariton condensation in colloidal CdSe/CdS core/shell nanoplatelets. *Adv. Sci.* **9**, 2200395 (2022).
212. Bujalance, C. et al. Strong light–matter coupling in lead halide perovskite quantum dot solids. *ACS Nano* **18**, 4922–4931 (2024).
213. Mao, D. et al. Observation of transition from superfluorescence to polariton condensation in CsPbBr$_3$ quantum dots film. *Light-Sci. Appl.* **13**, 34 (2024).
214. Georgakilas, I. et al. Room-temperature cavity exciton-polariton condensation in perovskite quantum dots. *Nat. Commun.* **16**, 5228 (2025).
215. Accanto, N. et al. Engineering the spin-flip limited exciton dephasing in colloidal CdSe/CdS quantum dots. *ACS Nano* **6**, 5227–5233 (2012).
216. Becker, M. A. et al. Long exciton dephasing time and coherent phonon coupling in CsPbBr$_2$Cl perovskite nanocrystals. *Nano Lett.* **18**, 7546–7551 (2018).
217. Naeem, A. et al. Giant exciton oscillator strength and radiatively limited dephasing in two-dimensional platelets. *Phys. Rev. B* **91**, 121302 (2015).
218. Utzat, H. et al. Coherent single-photon emission from colloidal lead halide perovskite quantum dots. *Science* **363**, 1068–1072 (2019).
219. Rainò, G. et al. Superfluorescence from lead halide perovskite quantum dot superlattices. *Nature* **563**, 671–675 (2018).
Demonstration of superfluorescence as a collective enhancement of the emission rate in supercrystals of CsPbB$_3$ nanocrystals.

220. Zhou, C. et al. Cooperative excitonic quantum ensemble in perovskite-assembly superlattice microcavities. *Nat. Commun.* **11**, 329 (2020).
221. Cherniukh, I. et al. Perovskite-type superlattices from lead halide perovskite nanocubes. *Nature* **593**, 535–542 (2021).
222. Wang, F. D., Tang, R. & Buhro, W. E. The trouble with TOPO; identification of adventitious impurities beneficial to the growth of cadmium selenide quantum dots, rods, and wires. *Nano Lett.* **8**, 3521–3524 (2008).
223. Baranov, D. et al. Purification of oleylamine for materials synthesis and spectroscopic diagnostics for trans isomers. *Chem. Mater.* **31**, 1223–1230 (2019).
224. Carbone, L. et al. Multiple wurtzite twinning in CdTe nanocrystals induced by methylphosphonic acid. *J. Am. Chem. Soc.* **128**, 748–755 (2006).
225. Liu, H. T., Owen, J. S. & Alivisatos, A. P. Mechanistic study of precursor evolution in colloidal group II–VI semiconductor nanocrystal synthesis. *J. Am. Chem. Soc.* **129**, 305–312 (2007).
226. Garcia-Rodriguez, R., Hendricks, M. P., Cossairt, B. M., Liu, H. T. & Owen, J. S. Conversion reactions of cadmium chalcogenide nanocrystal precursors. *Chem. Mater.* **25**, 1233–1249 (2013).
227. Luo, B., Rossini, J. E. & Gladfelter, W. L. Zinc oxide nanocrystals stabilized by alkylammonium alkylcarbamates. *Langmuir* **25**, 13133–13141 (2009).
228. Duong, T. M. et al. Practice of electron microscopy on nanoparticles sensitive to radiation damage: $CsPbBr_3$ nanocrystals as a case study. *Front. Chem.* **10**, 1058620 (2022).
229. Hassinen, A. et al. Short-chain alcohols strip X-type ligands and quench the luminescence of PbSe and CdSe quantum dots, acetonitrile does not. *J. Am. Chem. Soc.* **134**, 20705–20712 (2012).
230. Bals, S., Liz-Marzán, L. M., Parak, W. J., Willets, K. A. & Xin, H. L. Best practices for using microscopy data in manuscripts: from pretty pictures to scientific evidence. *ACS Nano* **18**, 13453–13457 (2024).
231. Murphy, C. J. & Buriak, J. M. Best practices for the reporting of colloidal inorganic nanomaterials. *Chem. Mater.* **27**, 4911–4913 (2015).
232. Green, M. A. et al. Solar cell efficiency tables (version 63). *Prog. Photovolt. Res. Appl.* **32**, 3–13 (2024).
233. Schiettecatte, P., Mertens, S., Giordano, L., Vandewal, K. & Hens, Z. Accurate, precise, and verifiable photoluminescence efficiency of colloidal quantum dots sols by photothermal threshold quantum yield analysis. *Chem. Mater.* **37**, 17–25 (2025).
234. Chen, Z. et al. Large scale synthesis of red-emitting quantum dots for efficient and stable light-emitting diodes. *Adv. Mater.* **37**, 2413978 (2025).
235. Zhu, D. X. et al. Boosting the photoluminescence efficiency of InAs nanocrystals synthesized with aminoarsine via a ZnSe thick-shell overgrowth. *Adv. Mater.* **35**, e2303621 (2023).
236. Tanghe, I. et al. Optical gain and lasing from bulk cadmium sulfide nanocrystals through bandgap renormalization. *Nat. Nanotechnol.* **18**, 1423–1429 (2023).
237. Shockley, W. On the surface states associated with a periodic potential. *Phys. Rev.* **56**, 317–323 (1939).
238. Chang, J. H. et al. Unraveling the origin of operational instability of quantum dot based light-emitting diodes. *ACS Nano* **12**, 10231–10239 (2018).
239. Albaladejo-Siguan, M. et al. Stability of quantum dot solar cells: a matter of (life)time. *Adv. Energy Mater.* **11**, 2003457 (2021).
240. de Bruin, T. A. et al. Analysis of the 1 year outdoor performance of quantum dot luminescent solar concentrators. *Solar RRL* **7**, 2201121 (2023).
241. Edel, J. B., Fortt, R., deMello, J. C. & deMello, A. J. Microfluidic routes to the controlled production of nanoparticles. *Chem. Commun.* **21**, 1136–1137 (2002).
242. Yen, B. K. H., Stott, N. E., Jensen, K. F. & Bawendi, M. G. A continuous-flow microcapillary reactor for the preparation of a size series of CdSe nanocrystals. *Adv. Mater.* **15**, 1858–1862 (2003).
243. Lignos, I. et al. Synthesis of cesium lead halide perovskite nanocrystals in a droplet-based microfluidic platform: fast parametric space mapping. *Nano Lett.* **16**, 1869–1877 (2016).
244. Kubendhiran, S., Bao, Z., Dave, K. & Liu, R.-S. Microfluidic synthesis of semiconducting colloidal quantum dots and their applications. *ACS Appl. Nano Mater.* **2**, 1773–1790 (2019).
245. Xu, R. H. J., Keating, L. P., Vikram, A., Shim, M. & Kenis, P. J. A. Understanding hot injection quantum dot synthesis outcomes using automated high-throughput experiment platforms and machine learning. *Chem. Mater.* **36**, 1513–1525 (2024).
246. Chan, E. M. et al. Reproducible, high-throughput synthesis of colloidal nanocrystals for optimization in multidimensional parameter space. *Nano Lett.* **10**, 1874–1885 (2010).
247. Munyebvu, N., Lane, E., Grisan, E. & Howes, P. D. Accelerating colloidal quantum dot innovation with algorithms and automation. *Mater. Adv.* **3**, 6950–6967 (2022).
248. Hens, Z. & De Roo, J. Atomically precise nanocrystals. *J. Am. Chem. Soc.* **142**, 15627–15637 (2020).
249. Orfield, N. J., McBride, J. R., Keene, J. D., Davis, L. M. & Rosenthal, S. J. Correlation of atomic structure an photoluminescence of the same quantum dot: pinpointing surface and internal defects that inhibit photoluminescence. *ACS Nano* **9**, 831–839 (2015).
250. Chmiela, S. et al. Accurate global machine learning force fields for molecules with hundreds of atoms. *Sci. Adv.* **9**, eadf0873 (2023).
251. Chen, O. et al. Compact high-quality CdSe-CdS core–shell nanocrystals with narrow emission linewidths and suppressed blinking. *Nat. Mater.* **12**, 445–451 (2013).
Demonstration of CdSe/CdS quantum dots with (near) unity photoluminescence quantum yield. Key step for all quantum dot applications involving light emission, including single quantum dot devices.
252. Gao, Y. & Peng, X. Photogenerated excitons in plain core CdSe nanocrystals with unity radiative decay in single channel: the effects of surface and ligands. *J. Am. Chem. Soc.* **137**, 4230–4235 (2015).
253. Fu, Y. et al. Excellent stability of thicker shell CdSe@ZnS/ZnS quantum dots. *RSC Adv.* **7**, 40866–40872 (2017).
254. Protesescu, L. et al. Nanocrystals of cesium lead halide perovskites ($CsPbX_3$, X=Cl, Br, and I): novel optoelectronic materials showing bright emission with wide color gamut. *Nano Lett.* **15**, 3692–3696 (2015).
First synthesis, to the best of our knowledge, of $CsPbX_3$ nanocrystals with emission across the entire visible spectrum. Initiated vast research activities on these materials.
255. Koscher, B. A., Swabeck, J. K., Bronstein, N. D. & Alivisatos, A. P. Essentially trap-free $CsPbBr_3$ colloidal nanocrystals by postsynthetic thiocyanate surface treatment. *J. Am. Chem. Soc.* **139**, 6566–6569 (2017).
256. Maes, J. et al. Light absorption coefficient of $CsPbBr_3$ perovskite nanocrystals. *J. Phys. Chem. Lett.* **9**, 3093–3097 (2018).
257. Gao, M. et al. Bulk-like ZnSe quantum dots enabling efficient ultranarrow blue light-emitting diodes. *Nano Lett.* **21**, 7252–7260 (2021).
258. Xie, R., Rutherford, M. & Peng, X. Formation of high-quality I–III–VI semiconductor nanocrystals by tuning relative reactivity of cationic precursors. *J. Am. Chem. Soc.* **131**, 5691–5697 (2009).
259. Li, H., Jiang, X., Wang, A., Chu, X. & Du, Z. Simple synthesis of $CuInS_2$/ZnS core/shell quantum dots for white light-emitting diodes. *Front. Chem.* **8**, 669 (2020).
260. Green, P. B. et al. Controlling cluster intermediates enables the synthesis of small PbS nanocrystals with narrow ensemble line widths. *Chem. Mater.* **32**, 4083–4094 (2020).
261. Killilea, N. et al. Pushing PbS/metal-halide-perovskite core/epitaxial-ligand-shell nanocrystal photodetectors beyond 3 μM wavelength. *Adv. Funct. Mater.* **29**, 1807964 (2019).
262. Justo, Y. et al. Optical properties of PbS/CdS core/shell quantum dots. *J. Phys. Chem. C* **117**, 20171–20177 (2013).
263. Kim, T., Park, S. & Jeong, S. Diffusion dynamics controlled colloidal synthesis of highly monodisperse InAs nanocrystals. *Nat. Commun.* **12**, 3013 (2021).
264. Xie, R., Chen, K., Chen, X. & Peng, X. InAs/InP/ZnSe core/shell/shell quantum dots as near-infrared emitters: bright, narrow-band, non-cadmium containing, and biocompatible. *Nano Res.* **1**, 457–464 (2008).
265. Roshan, H. et al. Near infrared light-emitting diodes based on colloidal InAs/ZnSe core/thick-shell quantum dots. *Adv. Sci.* **11**, 2400734 (2024).
266. Prado, Y. et al. Seeded growth of HgTe nanocrystals for shape control and their use in narrow infrared electroluminescence. *Chem. Mater.* **33**, 2054–2061 (2021).
267. De Geyter, B. & Hens, Z. The absorption coefficient of PbSe/CdSe core/shell colloidal quantum dots. *Appl. Phys. Lett.* **97**, 161908 (2010).
268. Brokmann, X., Coolen, L., Dahan, M. & Hermier, J. P. Measurement of the radiative and nonradiative decay rates of single CdSe nanocrystals through a controlled modification of their spontaneous emission. *Phys. Rev. Lett.* **93**, 107403 (2004).
269. Klimov, V. I., Mikhailovsky, A. A., McBranch, D. W., Leatherdale, C. A. & Bawendi, M. G. Quantization of multiparticle Auger rates in semiconductor quantum dots. *Science* **287**, 1011–1013 (2000).
270. Fisher, B. R., Eisler, H.-J., Stott, N. E. & Bawendi, M. G. Emission intensity dependence and single-exponential behavior in single colloidal quantum dot fluorescence lifetimes. *J. Phys. Chem. B* **108**, 143–148 (2004).
271. Biadala, L., Louyer, Y., Tamarat, P. & Lounis, B. Direct observation of the two lowest exciton zero-phonon lines in single CdSe/ZnS nanocrystals. *Phys. Rev. Lett.* **103**, 4 (2009).
272. Masia, F., Accanto, N., Langbein, W. & Borri, P. Spin-flip limited exciton dephasing in CdSe/ZnS colloidal quantum dots. *Phys. Rev. Lett.* **108**, 087401 (2012).
273. Brokmann, X., Giacobino, E., Dahan, M. & Hermier, J. P. Highly efficient triggered emission of single photons by colloidal CdSe/ZnS nanocrystals. *Appl. Phys. Lett.* **85**, 712–714 (2004).
274. Spinicelli, P. et al. Bright and grey states in CdSe–CdS nanocrystals exhibiting strongly reduced blinking. *Phys. Rev. Lett.* **102**, 136801 (2009).
275. Biadala, L. et al. Tuning energy splitting and recombination dynamics of dark and bright excitons in CdSe/CdS dot-in-rod colloidal nanostructures. *J. Phys. Chem. C* **118**, 22309–22316 (2014).
276. Bae, W. K. et al. Controlled alloying of the core–shell interface in CdSe/CdS quantum dots for suppression of Auger recombination. *ACS Nano* **7**, 3411–3419 (2013).
277. Morozov, S. et al. Purifying single photon emission from giant shell CdSe/CdS quantum dots at room temperature. *Nanoscale* **15**, 1645–1651 (2023).
278. Sousa Velosa, F. et al. State filling and stimulated emission by colloidal InP/ZnSe core/shell quantum dots. *Adv. Opt. Mater.* **10**, 2200328 (2022).
279. Chandrasekaran, V. et al. Exciton dephasing by phonon-induced scattering between bright exciton states in InP/ZnSe colloidal quantum dots. *ACS Nano* **17**, 12118–12126 (2023).
280. Chandrasekaran, V. et al. Nearly blinking-free, high-purity single-photon emission by colloidal InP/ZnSe quantum dots. *Nano Lett.* **17**, 6104–6109 (2017).
281. Geiregat, P. et al. Using bulk-like nanocrystals to probe intrinsic optical gain characteristics of inorganic lead halide perovskites. *ACS Nano* **12**, 10178–10188 (2018).
282. Zhu, C. et al. Single-photon superradiance in individual caesium lead halide quantum dots. *Nature* **626**, 535–541 (2024).
283. Gilmore, R. H. et al. Epitaxial dimers and Auger-assisted detrapping in PbS quantum dot solids. *Matter* **1**, 250–265 (2019).
284. Masia, F., Langbein, W., Moreels, I., Hens, Z. & Borri, P. Exciton dephasing in lead sulfide quantum dots by X-point phonons. *Phys. Rev. B* **83**, 201309 (2011).

285. Krishnamurthy, S. et al. PbS/CdS quantum dot room-temperature single-emitter spectroscopy reaches the telecom O and S bands via an engineered stability. *ACS Nano* **15**, 575–587 (2021).
286. Brodu, A. et al. Exciton fine structure and lattice dynamics in InP/ZnSe core/shell quantum dots. *ACS Photon.* **5**, 3353–3362 (2018).
287. Dümbgen, K. C. *Fundamentals on the Synthesis, Shape and Surface Chemistry of Indium Phosphide Quantum Dots: Digging Deeper.* PhD thesis, Ghent Univ. (2023).
288. Guzelian, A. A. et al. Synthesis of size-selected, surface-passivated InP nanocrystals. *J. Phys. Chem.* **100**, 7212–7219 (1996).
289. Lee, Y. et al. Effectual interface and defect engineering for Auger recombination suppression in bright InP/ZnSeS/ZnS quantum dots. *ACS Appl. Mater. Interfaces* **14**, 12479–12487 (2022).
290. Michler, P. et al. Quantum correlation among photons from a single quantum dot at room temperature. *Nature* **406**, 968–970 (2000).
291. De Roo, J. The surface chemistry of colloidal nanocrystals capped by organic ligands. *Chem. Mater.* **35**, 3781–3792 (2023).
292. Hassinen, A., Moreels, I., Donega, C. D., Martins, J. C. & Hens, Z. Nuclear magnetic resonance spectroscopy demonstrating dynamic stabilization of CdSe quantum dots by alkylamines. *J. Phys. Chem. Lett.* **1**, 2577–2581 (2010).
293. Dümbgen, K. C. et al. Surface chemistry of InP quantum dots, amine–halide co-passivation, and binding of Z-type ligands. *Chem. Mater.* **35**, 1037–1046 (2023).
294. Leemans, J. et al. Acid–base mediated ligand exchange on near-infrared absorbing, indium-based III–V colloidal quantum dots. *J. Am. Chem. Soc.* **143**, 4290–4301 (2021).
295. De Roo, J. et al. Highly dynamic ligand binding and light absorption coefficient of cesium lead bromide perovskite nanocrystals. *ACS Nano* **10**, 2071–2081 (2016).
296. Grigel, V. et al. The surface chemistry of colloidal HgSe nanocrystals, toward stoichiometric quantum dots by design. *Chem. Mater.* **30**, 7637–7647 (2018).
297. Green, P. B. et al. PbS nanocrystals made using excess lead chloride have a halide-perovskite-like surface. *Chem. Mater.* **33**, 9270–9284 (2021).
298. De Roo, J., De Keukeleere, K., Hens, Z. & Van Driessche, I. From ligands to binding motifs and beyond; the enhanced versatility of nanocrystal surfaces. *Dalton Trans.* **45**, 13277–13283 (2016).

Acknowledgements

I.I., P.B.G., S.B. and Z.H. acknowledged the European Commission for funding (MSCA-DN Track The Twin, grant agreement 101168820). Z.H. acknowledges funding from the FWO-Vlaanderen (research projects G0B2921N and G0C5723N) and Ghent University (BOF-GOA 01G02124). Work performed at the Center for Nanoscale Materials, a US Department of Energy, Office of Science User Facility, was supported by the US DOE, Office of Basic Energy Sciences, under contract no. DE-AC02-06CH11357. J.S.O. acknowledges support from the NSF Center Integration of Modern Optoelectronic Materials on Demand (IMOD), NSF grant no. DMR-2019444.

Author contributions

Introduction (Z.H.); Experimentation (J.S.O., P.B.G. and Z.H.); Results (I.I., P.B.G., R.D.S., S.B. and Z.H.); Applications (A.J.H., E.H.S., S.Z. and Z.H.); Reproducibility and data deposition (A.J.H., J.S.O., S.B. and Z.H.); Limitations and optimizations (A.J.H., J.S.O. and Z.H.); Outlook (all authors); overview of the Primer (all authors).

Competing interests

The authors declare no competing interests.

Additional information

Supplementary information The online version contains supplementary material available at https://doi.org/10.1038/s43586-025-00413-y.

Peer review information *Nature Reviews Methods Primers* thanks Xin Tong and the other, anonymous, reviewer(s) for their contribution to the peer review of this work.

---

[1]Optoelectronic Materials Section, Faculty of Applied Sciences, Delft University of Technology, Delft, The Netherlands. [2]Department of Chemistry, Northwestern University, Evanston, IL, USA. [3]Department of Electrical and Computer Engineering, University of Toronto, Toronto, Ontario, Canada. [4]BCMaterials, Basque Center for Materials, Applications and Nanostructures, Leioa, Spain. [5]Ikerbasque Basque Foundation for Science, Bilbao, Spain. [6]Department of Chemistry, Columbia University, New York, NY, USA. [7]Physics and Chemistry of Nanostructures, Department of Chemistry, Ghent University, Gent, Belgium. [8]Center of Nano- and Biophotonics, Ghent University, Ghent, Belgium. [9]Center for Nanoscale Materials, Argonne National Laboratory, Lemont, IL, USA. [10]EMAT, University of Antwerp, Antwerp, Belgium. [11]NANOlab Center of Excellence, University of Antwerp, Antwerp, Belgium. [12]IBM Research Europe — Zurich, Rüschlikon, Switzerland.